https://doi.org/10.5194/acp-2020-444
Preprint. Discussion started: 8 July 2020


Atmospheric Chemistry and Physics
Discussions

**Interaction of Dust Aerosols with Land/Sea Breezes over the Eastern Coast of the Red Sea from LIDAR Data and High-resolution WRF-Chem Simulations**

Sagar P. Parajuli[1*], Georgiy L. Stenchikov[1], Alexander Ukhov[1], Illia Shevchenko[1], Oleg Dubovik[2], and Anton Lopatin[3]

[1]King Abdullah University of Science and Technology, Thuwal, Saudi Arabia

[2]Univ. Lille, CNRS, UMR 8518 - LOA - Laboratoire d'Optique Atmosphérique, F-59000 Lille, France

[3]GRASP-SAS, Remote Sensing Developments, Université de Lille, Villeneuve D' ASCQ, 59655, France

[*]Corresponding Author, E-mail: psagar@utexas.edu

https://doi.org/10.5194/acp-2020-444
Preprint. Discussion started: 8 July 2020


Atmospheric Chemistry and Physics Discussions

**Abstract**

With advances in modeling approaches and the application of satellite and ground-based data in dust-related research, our understanding of the dust cycle has significantly improved in recent decades. However, two aspects of the dust cycle, namely the vertical profiles and diurnal cycles, are not yet adequately understood, mainly due to the sparsity of direct observations. Measurements of backscattering caused by atmospheric aerosols have been ongoing since 2014 at the King Abdullah University of Science and Technology (KAUST) campus using a micro-pulse LIDAR with a high temporal resolution. KAUST is located on the east coast of the Red Sea (22.3° N, 39.1° E), and currently hosts the only operating LIDAR system in the Arabian Peninsula. We use the data from this LIDAR together with other collocated observations and high-resolution WRF-Chem model simulations to study the following aspects of aerosols, with a focus on dust over the Red Sea Arabian coastal plains. Firstly, we investigate the vertical profiles of aerosol extinction and concentration in terms of their seasonal and diurnal variability. Secondly, we evaluate how well the WRF-Chem model performs in representing the vertical distribution of aerosols over the study site. Thirdly, we explore the interactions between dust aerosols and land/sea breezes, which are the most influential components of the local diurnal circulation in the region. We found a substantial variation in the vertical profile of aerosols in different seasons. We also discovered a marked difference in the daytime and nighttime vertical distribution of aerosols at the study site, as revealed by the LIDAR data. The LIDAR data also identified a prominent dust layer at ~5–7 km during the nighttime, which represented the long-range transported dust brought to the site by the easterly flow from remote inland deserts. The vertical profiles of aerosol extinction in different seasons were largely consistent between the LIDAR, MERRA-2 reanalysis, and CALIOP data, as well as in the WRF-Chem simulations. The sea breeze circulation was much deeper (~2 km) than the land breeze circulation (~1 km), but both breeze systems prominently affected the distribution of dust aerosols over the study site. We observed that sea breezes push the dust aerosols upwards along the western slope of the Sarawat Mountains, which eventually collide with the dust-laden northeasterly trade winds coming from nearby inland deserts, causing elevated dust maxima at a height of ~1.5 km above sea level over the mountains. Moreover, the sea and land breezes intensified dust emissions from the coastal region during the daytime and nighttime, respectively. The WRF-Chem model successfully captured the onset, demise, and height of a large-scale dust event that occurred in 2015, compared to LIDAR data. Our study, although focused on a particular region, has broader environmental implications as it highlights how aerosols and dust emissions from the coastal plains can affect the Red Sea climate and marine habitats.

## 1. Introduction

Dust aerosols, which mainly originate from natural deserts and disturbed soils such as agricultural areas, have implications for air quality (Prospero, 1999; Parajuli et al., 2019) and the Earth's climate (Sokolik and Toon, 1996; Mahowald et al., 2006; Prakash et al., 2014; Bangalath and Stenchikov, 2015; Kalenderski and Stenchikov, 2016; Di Biagio et al., 2017). The Arabian Peninsula represents a key area within the global dust belt where significant dust emissions take place in all seasons. However, the spatio-temporal characteristics of dust emissions in the region have not yet been fully described, partly because of the sparsity of observations. Although our understanding of the dust cycle and the related physical processes has substantially improved in recent decades (Shao et al., 2011), in the present context, two aspects of dust aerosol dynamics remain the least explored: the vertical structure and the diurnal cycle. Understanding the vertical structure is important because the vertical distribution of aerosols affects the radiative effects (Johnson et al., 2008; Osipov et al., 2015) and surface air quality (Chin et al., 2007; Wang et al., 2010; Ukhov et al., 2020). Similarly, understanding the diurnal cycle of aerosols is important because aerosols scatter and absorb radiation (Sokolik and Toon, 1998; Di Biagio et al., 2017), which ultimately affects the land and sea breezes. On the other hand, land and sea breezes, which are the key diurnal-scale atmospheric processes in the region, can also affect the distribution and transport of aerosols (Khan et al., 2015), as well as their composition (Fernández-Camacho et al., 2010; Derimian et al., 2017).

A micro-pulse LIDAR (MPL) has been operating at King Abdullah University of Science and Technology (KAUST), Thuwal, Saudi Arabia, since 2014. This LIDAR is collocated with the KAUST AERONET (Aerosol Robotic Network) station. The KAUST MPL site is a part of Micro-Pulse Lidar Network (MPLNET), maintained by NASA Goddard Space Flight Center (GSFC) (Welton et al., 2001). KAUST hosts the only LIDAR site in the Arabian Peninsula and its colocation with the AERONET station facilitates the retrieval of the vertical profile of aerosols more accurately. Stations that measure a range of parameters of interest for dust-related research are rare across the global dust belt. In addition to the LIDAR and AERONET station, KAUST also has a meteorological station that measures wind speed, air temperature, and incoming short-wave and long-wave radiative fluxes. These collocated data provide an opportunity to get a more complete picture of dust emissions and transport in the region.

Being located in an arid region, large-scale dust events are frequently experienced over the study site. However, satellite and ground-based observations such as AERONET have some limitations because of which they are likely to miss some important details of these dust events. For example, many large-scale dust events are accompanied by cloud cover, which restricts the retrieval of aerosol optical properties in the visible bands (Fernández et al., 2019). Extreme dust events are nonetheless important from a research perspective because they provide an opportunity to understand the associated physical processes. AERONET stations and passive satellite sensors are further limited because they cannot retrieve aerosol properties during the night. LIDARs help to overcome these limitations because they provide high-frequency measurements even in the night, and cloud cover does not directly affect their retrievals. Thus,

https://doi.org/10.5194/acp-2020-444
Preprint. Discussion started: 8 July 2020




LIDAR data are essential for understanding the diurnal variability of aerosols and their climatic effect.

The location of the Red Sea between the two key dust source regions of North Africa and the Arabian Peninsula provides a unique opportunity to understand the multi-faceted aspects of aerosol-climate interactions that occur in the region. KAUST is located on the eastern coast of the Red Sea, and dust is indeed the dominant aerosol type in this region (Prakash et al., 2014; Kalenderski and Stenchikov, 2016). The sea and land breezes that occur during the day and night, respectively, are the dominant drivers of local airmass circulations (Jiang et al., 2009). Sea breezes facilitate the transport of moisture inland and contribute to the formation of cumulus clouds and mesoscale convection (Davis et al., 2019). The land and sea breezes can themselves also generate dust emissions from the coastal regions (e.g., Crouvi et al., 2017), and also interact with atmospheric dust aerosols in multiple ways.

In this study, we attempt to understand the vertical and diurnal profiles of aerosols over the eastern coast of the Red Sea. We use our multiple collocated datasets collected at KAUST to shed light on the various facets of local-scale dust-climate interactions in the region. Since land and sea breezes are fine-scale features modulated by local topography, high-resolution simulations are essential to resolve these circulations. Therefore, we conduct high-resolution simulations using WRF-Chem to understand the nature of these circulations and their interaction with aerosols. In summary, we aim to answer the following specific research questions:

1. How are aerosols distributed in the vertical column over the study site at KAUST?
2. What is the seasonal or diurnal variability in the vertical distribution of aerosols?
3. How does WRF-Chem perform at representing the vertical distribution of aerosols over the study site?
4. How do prevailing land and sea breezes affect dust emissions and distribution over the study site?

This paper is organized as follows. We present a description of datasets and methods in section two, where we describe the observational datasets used and the WRF-Chem model settings applied. In section three, we present the results. More specifically, we explore the first and second research question listed above in section 3.2. Results presented in section 3.2 and 3.5 are relevant to the third research question. Section 3.4 addresses the fourth question. Finally, we present conclusions in section four, along with the limitations of our research and a more general discussion of the results.

## 2. Data and Methods

### 2.1. Study site

The KAUST campus is located in the western Arabian Peninsula, on the east coast of the Red Sea (22.3° N, 39.1° E). This area is affected by local dust storms originating from surrounding inland deserts, by non-local dust storms arriving from northeast Africa through the Tokar gap (see, for example, Kalenderski and Stenchikov 2016; Albugami et al., 2019; Kumar et al., 2019),

https://doi.org/10.5194/acp-2020-444
Preprint. Discussion started: 8 July 2020

Atmospheric Chemistry and Physics Discussions

and by dust from as far away as the Tigris-Euphrates regions (Parajuli et al., 2019). Therefore, dust is present in the atmosphere over the study site for most of the year.

Although our focus in this study is on dust aerosols, which are the dominant aerosol in the study site (Prakash et al., 2014; Parajuli et al., 2019), some additional aerosol types also contribute to the aerosol loading at KAUST. Our site is located on the coast; thus, sea salt aerosol, which is of natural origin, inevitably contributes considerably to the atmospheric aerosol loading. Furthermore, the study site has several industrial areas nearby that produce anthropogenic emissions of sulfur dioxide ($SO_2$), and black and organic carbon (BC and OC) (Ukhov et al., 2020a).

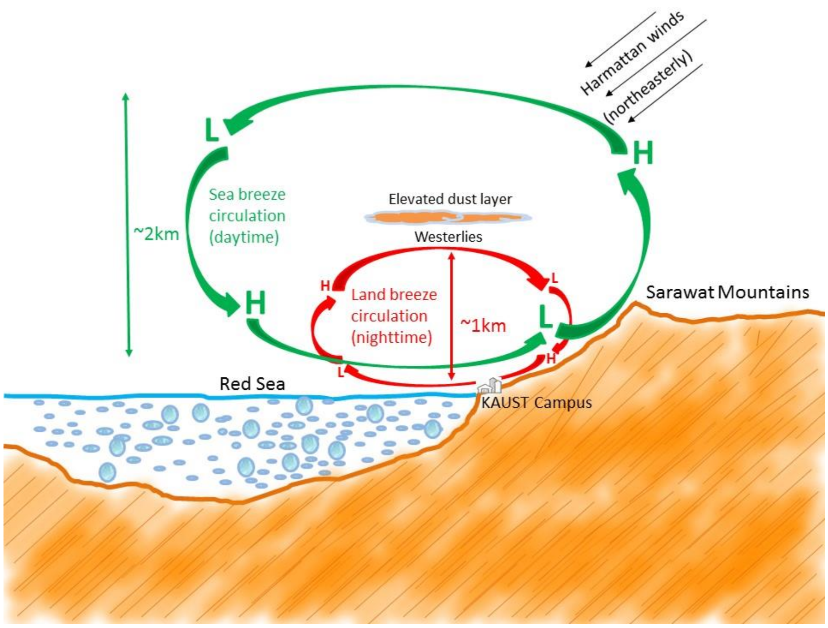


Figure 1. Schematic diagram showing sea breeze (daytime, in green) and land breeze (nighttime, in red) circulations and dust distribution over the study site at KAUST.

Because the site is located exactly at the land-ocean boundary, some unique small-scale processes exist that affect the local climate of this region. For instance, land and sea breezes affect the distribution of dust in the atmosphere over the study site. The desert land heats up during the day, which consequently heats the surface air above the land. This warm air mass rises due to convection, creating a local low pressure at the surface. The cooler and more moist air over the Red Sea then flows towards the low pressure, thus forming sea breezes (Simpson, 1994; Miller et al., 2003; Davis et al., 2019). During the night, this flow is reversed to form land breezes, when the land surface temperature cools quicker than the sea surface temperature. Because these breezes are driven by the thermal contrast between the land and the sea, their strengths vary by season. These breezes are further enhanced because of their coupling with slope winds that are generated on the Sarawat Mountains, which run along the western coast of the entire Arabian Peninsula (Davis et al., 2019). The salient features of the land and sea breezes over the study region are presented in Fig. 1, which we discuss in detail later.

### 2.2. Observations

We use several datasets, described below, to derive the climatology of the season profile and surface winds for the years 2015-2016.

***Datasets***

We collected meteorological data, including wind speed, temperature, and humidity from a tower established at KAUST in 2009 in collaboration with WHOI (Woods Hole Oceanographic Institution) (Farrar et al., 2009; Osipov et al., 2015).

We use cloud-free aerosol extinction profiles retrieved from a CALIOP (Cloud-Aerosol Lidar with Orthogonal Polarization) instrument onboard CALIPSO (Cloud-Aerosol Lidar and Infrared Pathfinder Satellite Observations) for analyzing the vertical structure of aerosols at the study site. CALIPSO is flown in a sun-synchronous polar orbit and is a part of NASA's Afternoon (A-train) constellations (Stephens et al., 2018). CALIOP acquires observations during both the day and night portion of the orbit with a 16-day repeat cycle. We use level-3 day/night aerosol data v3.00, which are monthly aerosol products generated by aggregating level-2 monthly statistics at 2° (lat) × 5° (long) resolution (Winker et al., 2013). The data have 208 vertical levels up to a height of 12 km above sea level.

We also analyze aerosol optical depth (AOD) data from AERONET station at KAUST (Holben et al., 1998). We use a level 2.0 version of directly measured AOD values (direct sun algorithm), which are cloud-screened and quality-assured. From AERONET, we also use an aerosol number density and a particle size distribution (PSD) obtained by inversion (Dubovik et al., 2000) to characterize the aerosol particles in the region. We use the AERONET V3, level 2.0 product, which provides volume concentration of aerosols in the atmospheric column in 22 bins between 0.05 and 15 microns in radius (Dubovik et al., 2000; Parajuli et al., 2019; Ukhov et al., 2020).

We use Moderate Resolution Imaging Spectroradiometer (MODIS) level-2 Deep Blue AOD data (Hsu et al., 2004), which are available daily, for the whole globe, at a resolution of ~ 0.1°× 0.1°. We use the latest version of the MODIS dataset (collection 6) (Hsu et al., 2013) because of its extended coverage and improved Deep Blue aerosol retrieval algorithm, compared to its earlier version (collection 5). We process AOD data of both Terra and Aqua satellites on a daily basis, and use the average of the two data products for our analysis. From MODIS, we also use the true color images for a qualitative analysis of a dust event.

We adopt the Modern-Era Retrospective Analysis for Research and Applications version 2 (MERRA-2) data (Rinecker et al., 2011) for comparing the model simulated AOD and dust concentrations. Aerosol data from the MERRA-2 dataset assimilate several satellite observations, including MODIS AOD (Gelaro et al., 2017). We specifically use tavg1_2d_aer_Nx and inst3_3d_aer_Nv products for getting 2-d AOD/DOD data and 3-D aerosol concentrations, respectively. MERRA-2 data consist of 72 vertical model levels between ~0.23 to 79.3 km.

We also employ 555nm column AOD from MISR onboard Terra satellite archived under collection MIL3DAE_4, which is a daily product available at 0.5x0.5 degree resolution (Diner, 2009). Because MISR has a wider view with nine viewing angles, MISR identifes thin aerosol layers more accurately and is more sensitive to the shape and size of particles (Kahn et al., 2005).

We also use the RGB composite from SEVIRI (Spinning Enhanced Visible and Infrared Imager) instrument onboard the geostationary Meteosat satellite, which is a composite prepared from specific infrared channels that are sensitive to the presence of dust in the atmosphere (Ackerman, 1997; Schepanski et al., 2007). Dust appears 'pink' in these composite images and is thus distinguishable from clouds, which are usually shown in yellow, red, or green.

***LIDAR data***

Micropulse LIDAR is a fully autonomous active remote-sensing system in which a laser transmitter emits light vertically upward, and an optical sensor receives the backscattered signals. The numbers and the detection time of the backscattered photons provide information about the aerosols and clouds in the atmosphere. The LIDAR located on the KAUST campus, which is also a part of the MPLNET network, operates at a wavelength of 532nm. The data from this LIDAR (hereafter called KAUST–MPL) is the main basis of this paper.

The colocation of the KAUST–MPL and AERONET station provides a more comprehensive microphysical picture when combined with AERONET sun-photometer measurements. We retrieve height-resolved aerosol properties, including aerosol extinction, absorption, and mixing ratios from the KAUST–MPL. We employ GRASP (Generalized Retrieval of Aerosol and Surface Properties, Dubovik et al., 2011, 2014), which is an open-source inversion code that combines different types of remote sensing measurements, such as radiometer and LIDAR observations, to generate fully consistent columnar and vertical aerosol properties (Lopatin et al., 2013).

We use cloud-screened AERONET radiances and LIDAR backscatter signals combined to retrieve aerosol properties during the daytime. As the AOD data are unavailable during the night, for nighttime retrievals, we use a so-called multi-pixel approach, first introduced by Dubovik et al. (2011) and realized in GRASP. According to this approach, retrieval is implemented for a group of observations coordinated in time or/and in space (e.g., several satellite pixels). Correspondingly, the quality of the retrievals can be improved by using some additional a priori constraints on the time-varying aspect of the retrieved parameters. For example, in this study, we invert the closest AERONET measurements obtained the day before and the day after, together with the nighttime LIDAR backscatter data, under some constraints on the temporal variability of columnar parameters (size distribution, complex refractive index, and sphericity fraction) provided by AERONET measurements. In contrast to other similar but simpler retrieval approaches used currently, multi-pixel concept constraints, but do not eliminate possible variability between parameters. For example, in this study, the implemented retrieval allows us to observe the variability of columnar properties during the night. In contrast, in similar retrieval realized by Benavent-Oltra et al. (2019), any variability of columnar properties through the night was not considered.

https://doi.org/10.5194/acp-2020-444
Preprint. Discussion started: 8 July 2020


Atmospheric Chemistry and Physics Discussions

The retrieved aerosol data has 100 levels in the vertical dimension with a resolution of 75m from 505m to 7700m above sea level. The processed LIDAR extinction data has some data gaps because of the quality constraints applied and cloud filtering. To achieve a complete diurnal picture, we also analyze the raw data of the normalized relative backscatter (NRB), which gives the total backscatter from both aerosols and clouds at a fine, 1-min resolution.

### 2.2. WRF-Chem model set up

We use WRF-Chem (v3.8.1) for simulating the emission and transport of dust and other aerosols at high resolution at the study site. The innermost domain (d03), which is marked by a red box in Fig. 2, is centered at KAUST and has a fine resolution of 1.33 km, which is required to resolve the essential features of local wind circulation and breezes. The innermost domain is encompassed by a second domain (d02) having a resolution of 4 km that covers the entire Arabian Peninsula. To allow full aerosol exchange and cover all major sources of dust in the region, we nested the two inner domains within a larger domain (d01) with 12 km resolution, which covers the entire MENA region shown in Fig. 2. The key physics and chemistry options used in WRF-Chem are presented in Table 1.

The model top is set at 100 hPa, and the model has 30 vertical levels between ~20 m to 16 km. To better represent winds, we apply 'grid nudging' on the u and v components of wind above the planetary boundary layer (PBL) in all three domains (Parajuli et al., 2019). We do not use any convective parameterization scheme and resolve deep convection in the innermost domain. We employ two-way nesting, which means that the parent domain provides boundary conditions for the nest, and the nest provides feedback to the parent domain. The model time steps are set to 72, 24, and 8 seconds for the three domains d01, d02, and d03, respectively.

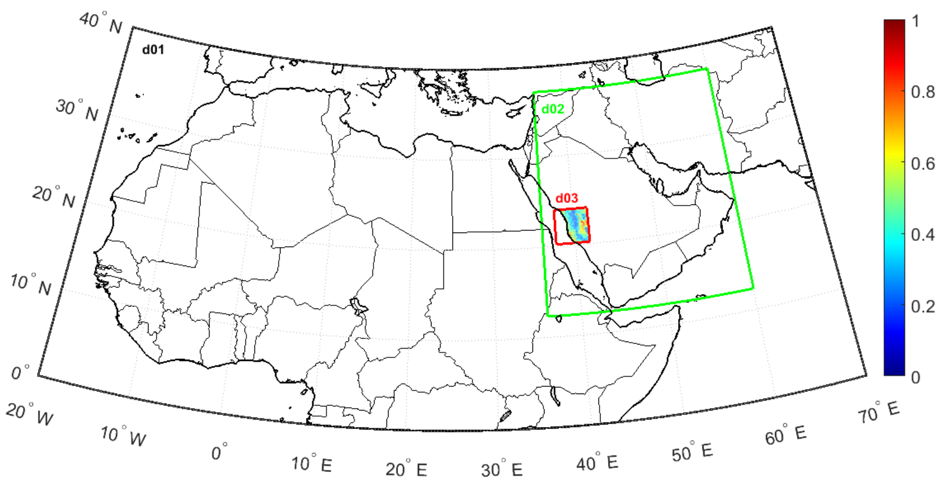


Figure 2. The study region over the Red Sea showing the three nests d01 (black), d02 (green), and d03 (red) used in WRF-Chem simulations. The base map within d03 shows the high-resolution dust source function (Parajuli and Zender, 2017) used in this study, in which the values range from zero to one with the highest value representing strongest dust source.

https://doi.org/10.5194/acp-2020-444
Preprint. Discussion started: 8 July 2020



Table 1. Details of key physics and chemistry namelist settings used in WRF-Chem.

| **Description** | | **Namelist Options** | **References** |
|---|---|---|---|
| **Physics** | Microphysics | mp_physics = 2 | Lin et al. scheme |
| | Planetary Boundary Layer (PBL) scheme | bl_pbl_physics = 2 | MYJ (Janjic, 1994) |
| | Surface layer physics | sf_sfclay_physics = 2 | Monin-Obukhov (Janjic Eta) |
| | Land Surface Model | sf_surface_physics = 2 | Unified Noah land surface model (Chen and Dudhia, 2001) |
| | Cumulus parameterization | cu_physics = 0 (turned off) | |
| | Radiative transfer model | ra_lw_physics = 4, ra_sw_physics = 4 | Rapid radiative transfer model (RRTMG) (Iacono et al., 2008) |
| **Chemistry** | Chemistry option | chem_opt = 301 | GOCART coupled with RACM-KPP |
| | Dust scheme | dust_opt = 3 | GOCART with AFWA changes (LeGrand et al., 2019) |
| | Photolysis scheme | phot_opt = 2 | Wild et al., 2000 |

We use high-resolution operational analysis data from ECMWF (~15 km) to provide initial and boundary conditions in our model, which are updated every 6 hours. The sea surface temperature (SST) values are also updated in our simulations, using the same ECMWF dataset.

We employ the Global Ozone Chemistry Aerosol Radiation and Transport (GOCART) aerosol scheme in our simulations (Chin et al., 2002). For calculating dust emissions, we use the AFWA dust scheme, which follows the original GOCART dust scheme (Ginoux et al., 2001) modified to account for saltation (LeGrand et al., 2019). It is important to represent the dust sources at a fine-scale to capture the smaller-scale physical processes accurately. Therefore, we use a recently developed high-resolution sediment supply map (SSM) as source function (Parajuli and Zender, 2017; Parajuli et al., 2019) in all three model domains. We adopt the tuning process of the dust model described in Parajuli et al. (2019). We tuned the model against CALIOP DOD and the same tuning coefficients obtained from Parajuli et al. (2019) are used in all domains, including the added third domain, which are 0.136, 0.196, 0.120, and 0.110, for DJF, MAM, JJA, and SON, respectively.

We consider dust, sea salt, sulfate, and black and organic carbon (BC and OC) aerosols in our simulations. Biomass burning and biogenic aerosols are not important over the region, and thus we do not include them.

Sea salt emissions in WRF-Chem follow the parameterization developed by Monahan et al., (1986) and Gong (2003). In this parameterization, the rate of sea salt emissions produced via whitecaps and wave disruption is given as a function of particle size and 10-m wind speed.

https://doi.org/10.5194/acp-2020-444
Preprint. Discussion started: 8 July 2020



We take the anthropogenic emissions of OC and BC from the most recent version of EDGAR (Emission Database for Global Atmospheric Research) database v4.3.2 available at 0.1°x0.1° resolution (Crippa et al., 2018). The EDGAR database is a global database that provides gridded emission maps of several greenhouse gases and air pollutants from 1970-2012. We use OC and BC emissions data from 2012.

Sulfur dioxide ($SO_2$) is of particular concern because it chemically transforms in the atmosphere into secondary sulfate, which is an important and influential aerosol at our study site (Ukhov et al., 2020a, Ukhov et al., 2020b). To achieve a more accurate representation of sulfate aerosols, we use the $SO_2$ emissions from a time-varying (monthly) inventory developed by NASA for the same year (2015). This $SO_2$ inventory is developed by combining satellite-based estimates from the ozone monitoring instrument (OMI) with the ground-based inventory developed by the Task Force Hemispheric Transport Air Pollution (HTAP) (Janssens-Maenhout et al., 2015), which provides a more accurate gridded emission dataset with greater spatial and temporal coverage. The data has global coverage with 0.1x0.1 degree resolution (Liu et al., 2018). This dataset does not account for $SO_2$ emissions produced by ships; therefore, we take ship $SO_2$ emissions from the EDGAR v4.3.2 dataset. OMI-HTAP emissions in WRF-Chem are satisfactorily reproduced by the observed $SO_2$ loading in the Middle East region (Ukhov et al., 2020a).

We activate both gas and aerosol chemistry in our simulations (gaschem_onoff = 1, aerchem_onoff = 1) and apply the aerosol chemistry options in all three domains.

To determine the contribution of each aerosol species on total AOD, we modify the WRF Chem code, mainly the Fortran files *optical_driver.F* and *chem_driver.F* located under the chem folder. For this purpose, we calculate aerosol optical properties twice, first with the mixture containing all aerosols and second after removing a specific aerosol. This calculation is implemented in the subroutine "*optical_averaging*". Thus, we obtain the contribution of specific aerosol species on total AOD by subtracting the AOD obtained without a specific aerosol from the total AOD calculated when all aerosols are accounted for.

We calculate the total aerosol concentration (TAC) in $\mu g\ m^{-3}$ by summing up the individual concentrations of all aerosol species, viz., dust, sea salt, sulfate ($SO_4$), OC, BC, and other components of PM. The equation used to calculate the total aerosol concentration from the standard output variables of WRF Chem is presented below.

TAC ($\mu g\ m^{-3}$) = [(DUST_1+DUST_2+DUST_3+DUST_4+DUST_5) + (SEAS_1+SEAS_2+SEAS_3+SEAS_4) + (OC1+OC2) + (BC1+BC2) + P10 + P25] × 1/ALT + sulf × 1/ALT × 1000 × 96/29.

where, DUST_1…DUST_5 are the dust mass mixing ratios ($\mu g\ kg^{-1}$) in five different size bins; SEAS_1….SEAS_4 are the sea salt mass mixing ratios ($\mu g\ kg^{-1}$) in four different size bins; P10 and P25 are other anthropogenic PM10 and PM2.5 mass mixing ratios ($\mu g\ kg^{-1}$), respectively; OC1 and BC1 are mass mixing ratios ($\mu g\ kg^{-1}$) of hydrophobic organic carbon and black carbon, respectively; OC2 and BC2 are mass mixing ratios ($\mu g\ kg^{-1}$) of hydrophilic organic carbon and black carbon, respectively; sulf is the $SO_4$ volume mixing ratio (ppmv), ALT is the

https://doi.org/10.5194/acp-2020-444
Preprint. Discussion started: 8 July 2020

Atmospheric Chemistry and Physics Discussions

inverse of air density ($m^3\ kg^{-1}$), and 96/29 is the ratio of the molecular weights ($g\ mol^{-1}$) of sulfate and air.

We conduct the model simulations for the entire year of 2015 on a monthly basis (for computational reasons). For each month, the model simulations start a week before the month begins, and we discard the data from this week as spin-up. We use data for 2015 only for the comparison of the model results with other datasets. However, we use the entire two years of data (2015-16) to derive the climatology. Because we aim to explore the diurnal cycles, we use hourly model output data for analysis. To compare the LIDAR and other station data with gridded datasets, we use data corresponding to a grid cell containing the KAUST site from all gridded datasets.

## 3. Results

### 3.1. Comparison of AOD and aerosol volume concentrations

Figure 3 shows the model-simulated time series of total columnar AOD at KAUST obtained using daily-average values, compared with several datasets, including AERONET, MODIS, MISR, and MERRA-2. For the model and MERRA-2 data, we only use the daytime data (between 7 AM and 7 PM local time) to make them consistent with AERONET, MODIS, and MISR data. In general, all data are consistent and show similar temporal patterns. The model reproduces the AOD time series well in all seasons. There is some mismatch in the AOD profiles among different datasets during some large-scale dust events, which is partly because of the difference in sampling and measurement frequencies among different datasets.

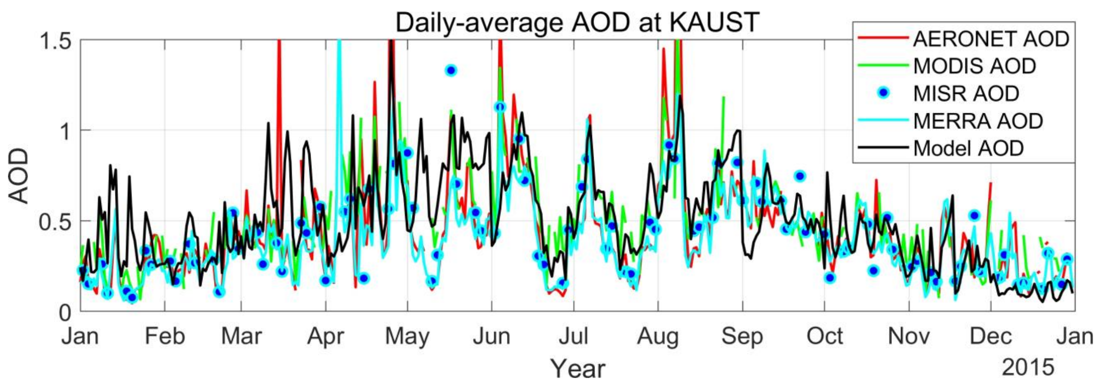


Figure 3. Time-series of daily-averaged AOD at KAUST (AERONET, MODIS, MERRA-2, and Model AODs at 550nm and MISR AOD at 555nm).

For a quantitative evaluation of the model results, we calculate the Mean bias error (MBE) of the model AOD against the three sets of observations, viz., AERONET, MODIS, and MISR at KAUST. The MBEs calculated using daily-mean values for 2015 are presented in Table 2. We also calculate the Pearson's correlation coefficient ($\rho$) of the simulated AOD against the available observations. The calculated MBE for the model is low against all datasets. The MBE is 13.4 % against the most-reliable AERONET data. The model AOD also shows a good

https://doi.org/10.5194/acp-2020-444
Preprint. Discussion started: 8 July 2020


Atmospheric Chemistry and Physics Discussions
Open Access
EGU

correlation with observations, with a correlation coefficient exceeding 0.6 for all datasets. These results demonstrate that the model simulated AOD values are robust.

Table 2. Statistics* of simulated AOD compared with different observations at KAUST.

| Dataset | AERONET | MODIS | MISR |
|---|---|---|---|
| **Pearson's correlation coefficient** $\rho$ ** | 0.61 | 0.63 | 0.71 |
| **Mean Bias Error (MBE)** | 0.059 | -0.008 | 0.063 |
| **Annual average AOD (Model AOD = 0.49)** | 0.44 | 0.47 | 0.43 |

*Calculated using daily-average data for 2015. **all correlation coefficients are significant ($p < 0.0001$).

Figure 4 shows the contribution of different aerosol species on total AOD at KAUST, as simulated by WRF-Chem. Dust is the major contributor to AOD in all seasons, reaching above 90 % in spring and summer. This result is consistent with earlier reported percentage contributions of dust over the region (Kalenderski et al., 2016). The anthropogenic contribution is highest in winter but contributes less than 15 %. The contribution of sea salt emissions is also small in all seasons (less than 10 %). These results are also qualitatively consistent with the contributions derived from CALIOP data that use histograms of aerosol type in a grid cell containing the KAUST site (Fig. S1).

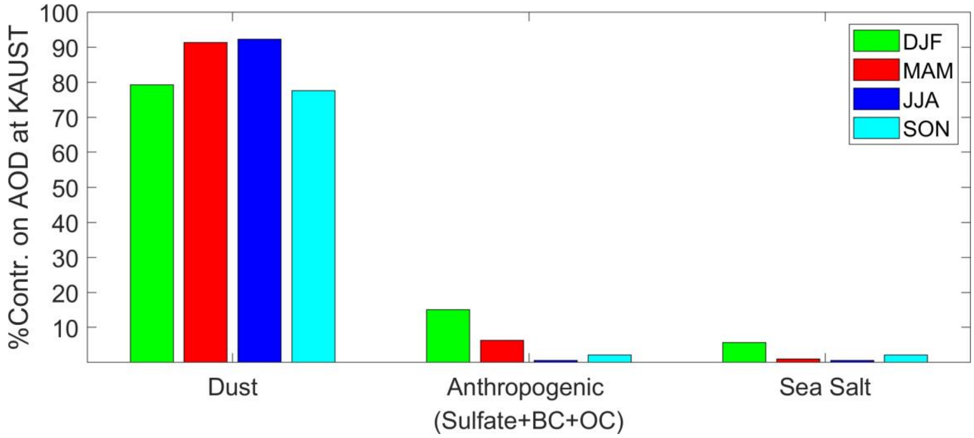


Figure 4. Percentage contribution of different aerosol types on total AOD at KAUST as simulated by WRF-Chem.

https://doi.org/10.5194/acp-2020-444
Preprint. Discussion started: 8 July 2020



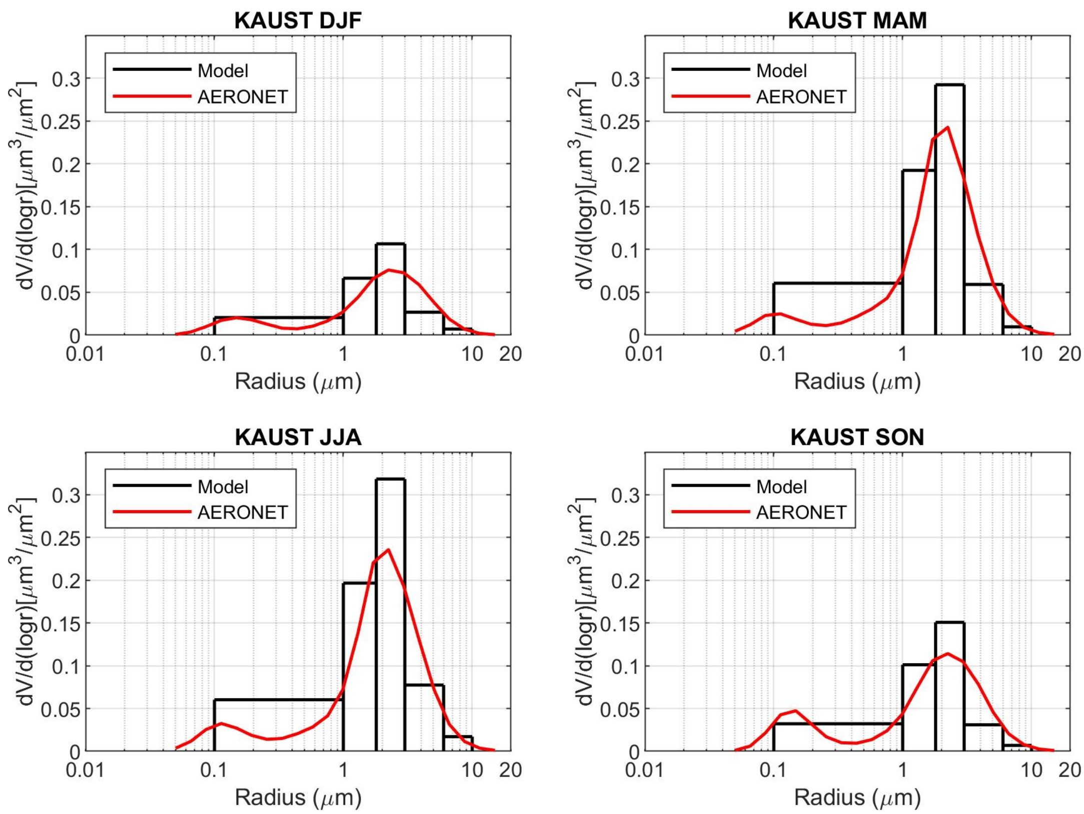


Figure 5. Column-integrated volume size distributions and concentrations of only dust from the model, plotted against AERONET aerosol volume concentrations at KAUST.

The size distributions of dust, sea salt, and sulfate are modeled in WRF-Chem using approximation over different size bin. Dust and sea salt are distributed in five and four size bins, respectively, both between 0.1 and 10 $\mu m$ radius, as detailed in Ukhov et al. (2020). Sulfate aerosols are distributed in two lognormal modes, Aitken and Accumulation. As discussed earlier, dust is the dominant aerosol type; thus, here we compare the volume size distributions of the modeled dust with the AERONET data. Figure 5 shows the column-integrated volume PSD in the model and AERONET data. The simulated and observed volume PSDs are reasonably well matched in all seasons even though the dust in the model is distributed in five bins only (Parajuli et al., 2019; LeGrand et al., 2019). Although the maximum radius of particles in AERONET data is 15 microns, which is larger than the maximum size in the model (10 microns), the majority of particles in the AERONET data fall within the 10-micron range. Recent measurements from aircraft have shown that dust particles can be much larger (Ryder et al., 2019), up to 40-micron in radius, during large-scale dust events (Marenco et al., 2018). However, the optical contribution of such large particles is relatively small. There are two distinct aerosol modes in AERONET PSD data: one finer mode centered around 0.1 microns, and another coarse mode centered around 2-3 microns. The coarse mode primarily corresponds to mineral dust (silt) that originates mainly from inland deserts, northeast Africa, and the Tigris-Euphrates source region.

https://doi.org/10.5194/acp-2020-444
Preprint. Discussion started: 8 July 2020




The composition of the fine mode is much more complex, but usually includes clay particles transported from long distances and anthropogenic aerosols from pollution sources (mainly as sulfate). The size distributions of sulfate and sea salt aerosols are presented in the supplementary information (Figs. S2 and S3). Note that we use the PSD and AOD data from this AERONET station (KAUST) to retrieve the LIDAR aerosol extinction profiles used in this study.

### 3.2. Surface Meteorology

Land and sea breezes affect dust aerosol emissions and transport in our study region. When the land and sea breezes are strong, they can cause dust emission from the active dust sources of the coastal regions. The land and sea breezes also transport the emitted dust either towards the ocean or towards the land, depending on the direction of the breeze. Moreover, land breezes can help to transport dust emitted from inland deserts and remote areas during large-scale dust events to the ocean (Prakash et al., 2014).

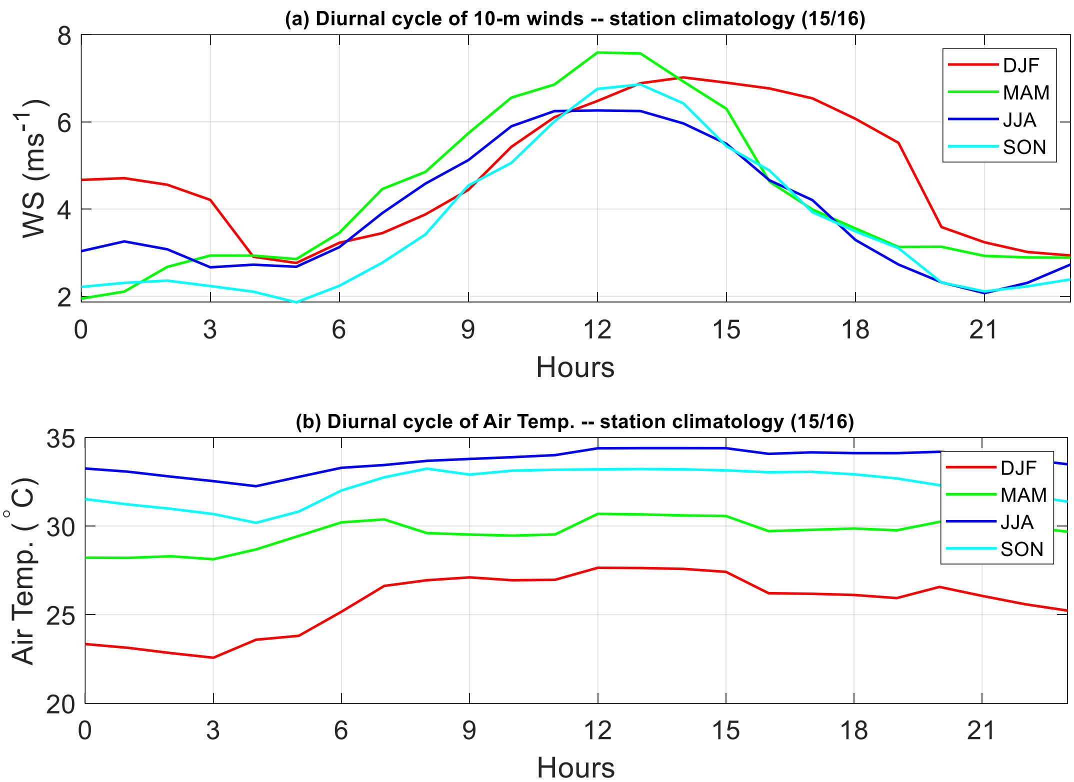


Figure 6. (a) Diurnal cycle climatology (2015/16) of surface winds and air temperature measured at KAUST station. Times are reported in UTC.

Because dust/aerosols are present over the study site for most of the year, they can also interact with the meteorology and thus affect atmospheric winds and temperature at different time scales.

Land and sea breezes are strongly coupled with dust/aerosols and temperature variability, especially near the surface.

Figure 6a shows the diurnal cycle climatology (2015/16) of station-measured surface wind speed at the study site. The surface winds reach a peak around noon UTC (15:00 local time) for all seasons except winter, consistent with the results of Davis et al. (2019). The aforementioned sea breezes cause these wind peaks in the afternoon. Note that these sea breezes originate at sea and advance landward to reach the coast only later in the afternoon (Estoque et al., 1961), where they are measured at our station. In winter, the wind speed profile shifts to the right, peaking later in the day at around 14:00 UTC. This shift to later in the day occurs because, in winter, it takes more time to reach the thermal contrast required between the land and the sea for the formation of sea breezes. Note the existence of a second peak in the wind speed plot during the night, around 01:00 UTC, which represents the land breezes. These land breezes are stronger in winter than in the other seasons.

The profiles of air temperature (Fig. 6b) are rather flat, showing a weak diurnal cycle. Winter shows the most pronounced diurnal cycle. The temperature contrast between day and night is minimal in summer and maximum in winter.

Given the strong diurnal cycles of surface winds and temperature, it is evident that the day and night circulation in the study area is remarkably different. Therefore, it becomes important to look at the aerosol vertical profiles separately in day and night time.

### 3.3. Vertical profiles

***Comparison of aerosol extinction profiles from KAUST–MPL with CALIOP data***

Figure 7 shows the comparison of aerosol extinction from KAUST–MPL and CALIOP, both of which show a similar profile. Most aerosols in the atmosphere are confined within the troposphere, below 8 km altitude, which is consistent in both datasets. However, the KAUST–MPL underestimates the extinctions near the surface compared to CALIOP data. Moreover, the nighttime dust events observed in the KAUST–MPL data are not present in the CALIOP data. These discrepancies could be related to the differences in algorithm and resolution, between the two datasets. Firstly, while retrieving aerosol extinction profiles, CALIOP algorithm uses an assumed extinction-to-backscatter (lidar ratio) for a set of aerosol types that are defined mostly geographically and on the base of raw lidar signal signatures (Kim et al., 2018). In contrast, the MPL algorithm assumes averaged lidar ratio for the whole column based on aerosol PSD, refractive index and sphericity, in such as way that it will satisfy both AERONET and MPL co-incident data. Secondly, KAUST–MPL is a point measurement that captures the temporal evolution of the dust storms better than CALIOP because it has a higher temporal resolution. For instance, CALIOP can undersample or overlook some dust events that last only for a few hours. On the other hand, CALIOP could sample more spatial details of a dust storm because it has a more extensive spatial coverage than the KAUST–MPL data. Nonetheless, these two datasets complement one another and their combined use can be beneficial in understanding the large-scale dust storms.

https://doi.org/10.5194/acp-2020-444
Preprint. Discussion started: 8 July 2020


Atmospheric Chemistry and Physics Discussions

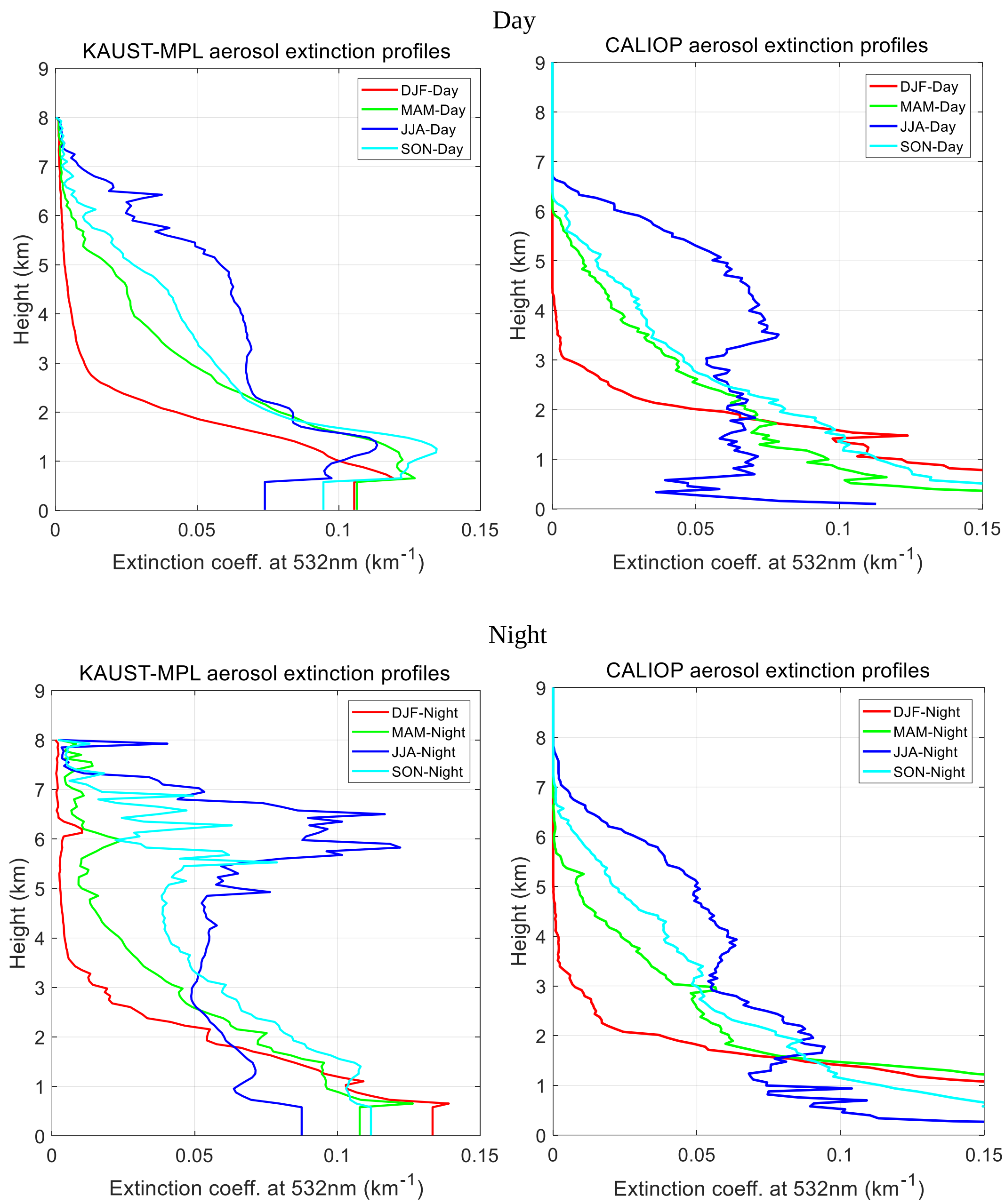


Figure 7. Comparison of seasonal climatology (15/16) of aerosol extinction from KAUST–MPL (left) and CALIOP (right) shown separately for day (upper two panels) and night (bottom two panels).

https://doi.org/10.5194/acp-2020-444
Preprint. Discussion started: 8 July 2020



Note that CALIOP extinction profiles represent data averaged over a large grid box (2x5 degree) that contains the KAUST site. As such, CALIOP represents the larger regional-scale vertical structure of aerosols compared to KAUST–MPL, which represents a more local structure. Above ~2 km, the profiles of the two datasets are much more similar, indicating the presence of a stable aerosol layer. This similarity is understandable because local fluctuations closer to ground level do not penetrate much above 2 km. Below ~2 km, there are more significant differences between the profiles. Note that the elevated aerosol loading present in the KAUST–MPL data at about 1 km height is not present in the CALIOP data. Nearer the surface, both CALIOP and KAUST–MPL have difficulty in retrieving the aerosol extinction, which is a common problem for all LIDARs (Koffi et al., 2012; Winker et al., 2013; Senghor et al., 2020).

***Comparison of extinction profiles between KAUST–MPL and model simulations***

Figure 8 shows the seasonally averaged vertical profiles of aerosol extinction from KAUST–MPL and model simulations, shown separately for day and night. The height of the top of the aerosol layer and the contrast of profiles in different seasons in the KAUST–MPL data and the model output are similar. The vertical profiles compare reasonably well, with similar orders of extinction in the daytime, especially considering the range of discrepancy in KAUST–MPL and CALIOP data that we discussed above. The magnitude of extinctions in the model and KAUST–MPL are in good agreement in the nighttime as well, except in summer and fall, in which cases the KAUST–MPL data shows higher extinctions, particularly above the PBL.

KAUST–MPL nighttime data show a distinct aerosol layer located between 5.5 and 7 km in summer and the fall. The model does not show such dust layers in the night. KAUST–MPL daytime data shows a typical elevated maxima of dust extinction in the PBL centered around 1.5 km altitude. However, the model does not identify such a dust loading profile. Note that the shape of the profile is reversed during the nighttime, which the model weakly reproduces. We explore this particularly interesting shape of the extinction profile at ~1–2 km in the daytime in section 3.4. As discussed later, these unique features of the profiles are related to the effect of land/sea breezes and topography.

https://doi.org/10.5194/acp-2020-444
Preprint. Discussion started: 8 July 2020

Atmospheric Chemistry and Physics
Discussions

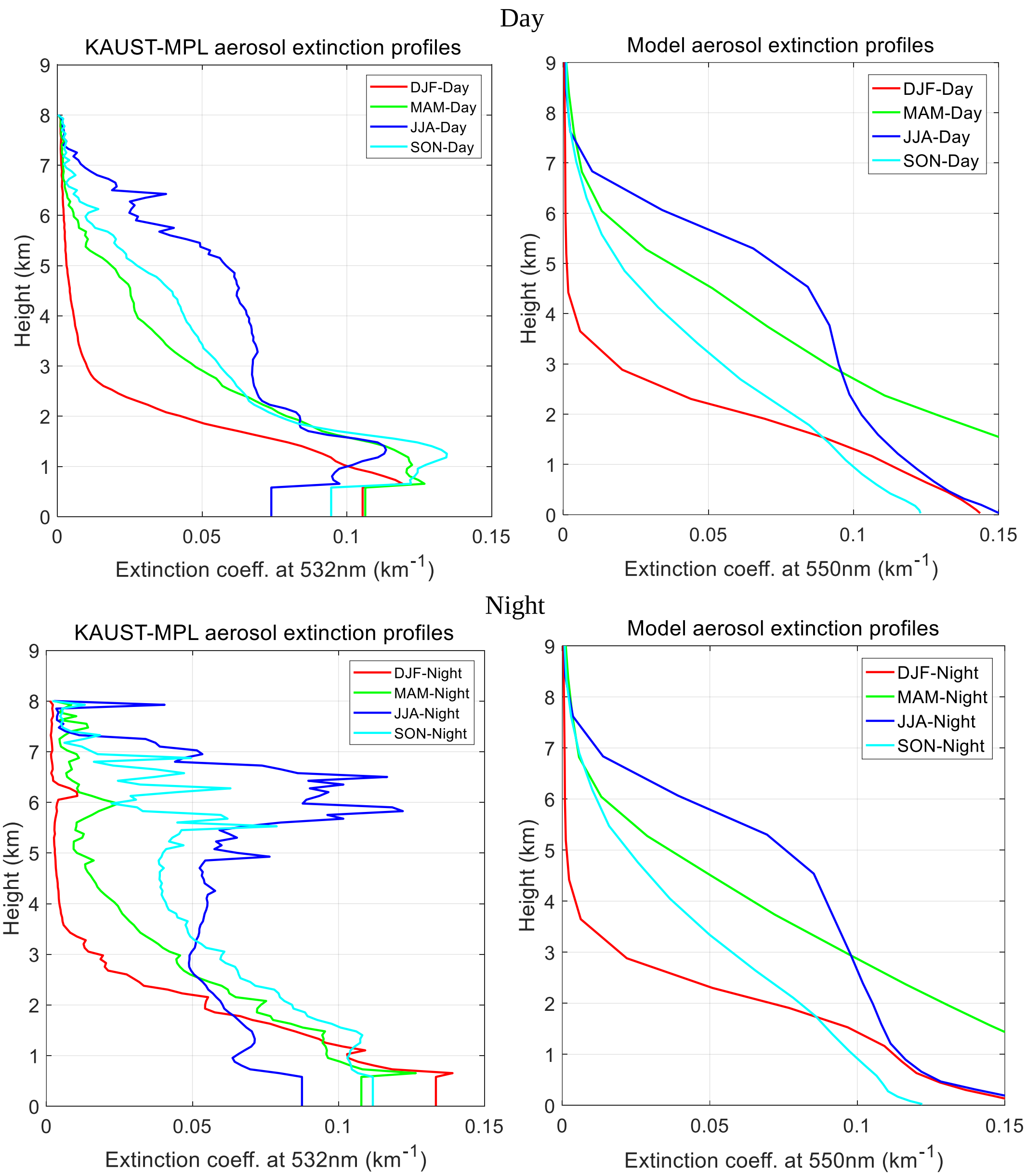


Figure 8. KAUST–MPL retrieved (left column) and model-simulated (right column) aerosol extinction profiles for different seasons presented separately for the daytime (upper two panels) and nighttime (bottom two panels). The measurement time of all KAUST–MPL data available for daytime fall between 05:00 and 15:00 UTC, and for nighttime data fall between 17:00 to 02:00 UTC. For the model, the day and nighttime data represent data between these times.

To understand the causes of the elevated dust maxima in the KAUST–MPL profiles at ~1–2 km altitude in the daytime and 5.5–7 km in the nighttime, we separately analyzed the profiles under

https://doi.org/10.5194/acp-2020-444
Preprint. Discussion started: 8 July 2020

Atmospheric Chemistry and Physics Discussions
Open Access
EGU

clear sky and dusty conditions. We define 'clear days' as the days with a daily mean of AOD at KAUST less than 0.25 and 'dusty days' as the days having daily-mean AOD greater than 0.75, using either MODIS AOD or AERONET AOD to maximize data availability during large-scale dust events. Figure 9 shows the average extinction profiles for clear and dusty conditions from KAUST–MPL data for 2015/16 obtained using these criteria. The profiles on dusty days differ remarkably from the profiles on clear days, both for the daytime and nighttime. During the daytime (Fig. 9, left), the maximum is even more prominent than in the profiles shown earlier in Fig. 7. Indeed, studies have shown that this shape is characteristic of dust profiles observed during large-scale dust events that occur near land-ocean boundaries (Khan et al., 2015; Senghor et al., 2017). Marenco et al. (2018) also observed a similarly elevated dust loading over the eastern Atlantic at a comparable height during the 'heavy dust' period of their flight.

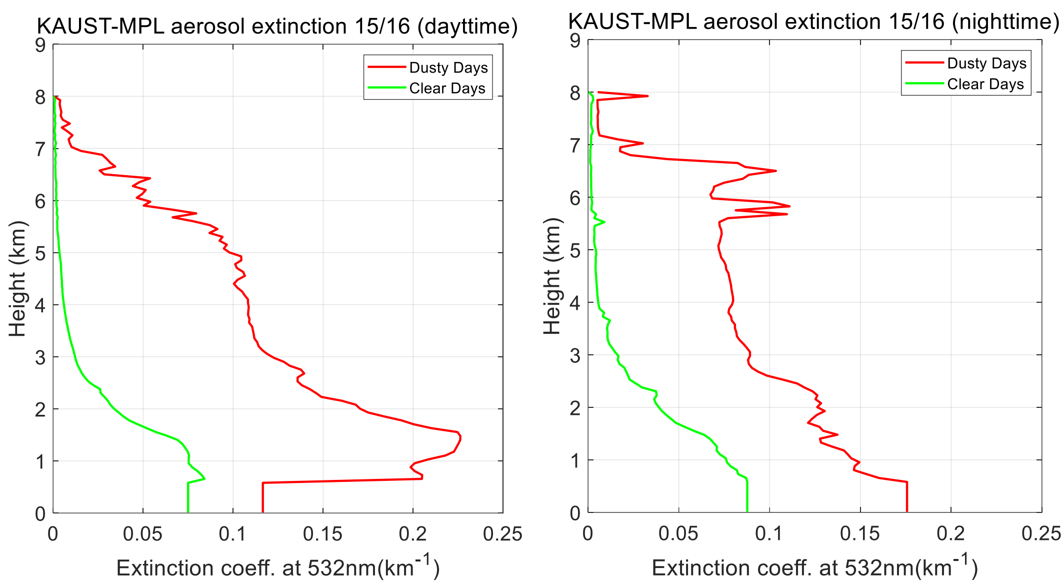


Figure 9. Average vertical profiles of aerosol extinction corresponding to 'clear days' and 'dusty days' from KAUST–MPL data.

The elevated dust layer during the nighttime at a height of 5.5–7 km observed earlier in summer and fall (Fig. 7) is present in the 'dusty days' and is absent in 'clear days' (Fig. 9, right). We suggest that these dust layers represent dust of non-local origin transported at higher altitudes during large-scale dust events. Next, we explore why such a high dust loading at this altitude in summer is present only in the nighttime and not in the daytime. Stronger convection in the inland desert regions during the daytime carries aerosols to higher altitudes. In the summer in deserts, convection is strongest in the afternoon, and the planetary boundary layer height (PBLH) can reach well above 5 km (Fig. S4). By the evening, the dust is mixed thoroughly within the PBL by this strong convection (Khan et al., 2015). At night, the PBL weakens and breaks the capping inversion, which allows the dust-laden layer from the PBL to mix into the free troposphere. The dust that lies above the PBL is ultimately carried to our site by the accelerated easterly

https://doi.org/10.5194/acp-2020-444
Preprint. Discussion started: 8 July 2020




geostrophic winds (Almazroui et al., 2018), which arrive at our site during the night. This process is evident if we look at the wind vectors at higher altitudes. As Fig. S5 shows, the winds are northeasterly below ~6 km, which are the regionally prevalent 'trade winds' commonly called Harmattans. Above ~6 km, the winds are easterly. These two wind patterns are thus responsible for the transport of dust from the inland deserts to the study site. The geostrophic wind transports dust at higher altitudes (6–7 km) and Harmattan transports dust at lower altitudes (1–2 km), which is why KAUST–MPL data shows elevated dust loading at these heights.

***Comparison of vertical profiles of dust concentrations***

Figure 10 shows the vertical profile of aerosol concentrations simulated by the model by seasons as compared with KAUST–MPL data and MERRA-2 reanalysis. The vertical profiles of aerosol concentrations from KAUST–MPL and the model largely resemble the extinction profiles presented earlier in Fig. 7. The variation in concentration profiles in different seasons is reasonably consistent in all three datasets. The elevated dust maxima at a height of ~1.5 km observed in the KAUST–MPL profiles is not present in the model or the MERRA-2 data. Both the model and MERRA-2 tend to overestimate aerosol concentrations compared to KAUST–MPL data in summer and in the lower atmosphere, particularly below 1 km. The model-simulated near-surface concentrations in summer are twice as large as those in the LIDAR data. This overestimation is counter-intuitive because the model AOD agrees well with AERONET AOD (Fig. 3) used to constrain LIDAR aerosol profiles. This discrepancy is related to the size distribution of particles. For AOD to be consistent in the model and LIDAR data, the model must overestimate the concentration of coarse particles in the lower atmosphere. Therefore, we can infer that the model overestimates the concentrations of coarse particles in the lower atmosphere relative to the observed concentrations.

In winter, the boundary layer is shallower, and the concentration profile resembles a typical profile that might be expected in a turbulent boundary layer, in which the concentration exponentially increases towards the surface, as observed in the field (e.g., Selezneva, 1966) and wind tunnel experiments (e.g., Neuman et al., 2009). In summer, the boundary layer is deeper, and the strong turbulent mixing transports dust higher into the atmosphere; consequently, the concentration profile is steeper.

During local dust events that originate in the nearby deserts, the atmospheric dust loading is mostly dominated by coarse-mode particles. In contrast, dust events of non-local origin carry long-range transported dust to the site, which typically constitute finer particles. Finer particles can easily reach the upper atmosphere, whereas coarser particles of higher mass fall back to the surface more quickly due to gravitational settling. Thus, coarser particles are usually confined to the lower atmosphere, have shorter atmospheric lifetimes (~1-3 days), and affect hourly/daily scale climate processes such as the diurnal cycle. On the contrary, smaller particles reach higher altitudes and have longer atmospheric lifetimes. The extinction cross-section of an individual large particle is bigger than that of a small particle, but finer particles have stronger radiative effects per unit mass than coarser particles (Khan et al., 2015).

https://doi.org/10.5194/acp-2020-444
Preprint. Discussion started: 8 July 2020



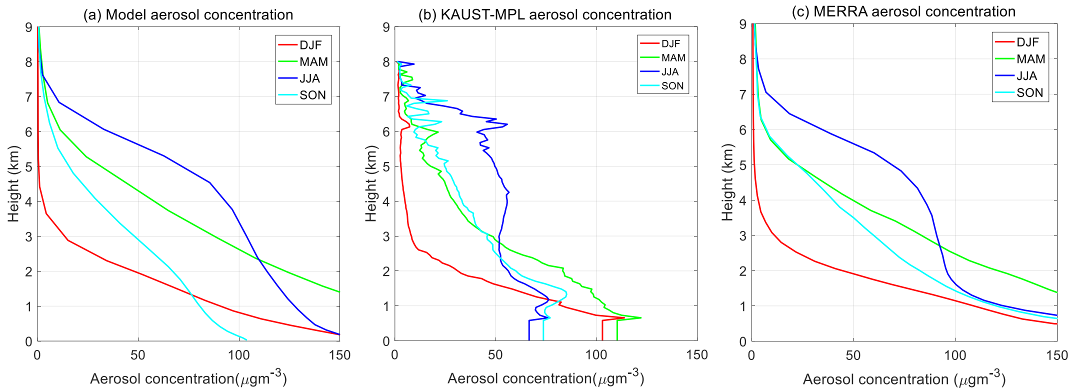


Figure 10. Comparison of vertical profiles of total aerosol concentrations among (a) the model (b) KAUST–MPL, and (c) MERRA-2 data for different seasons at KAUST.

### 3.3. Diurnal cycle

Figures 11a and 11b show the diurnal cycle of 10m wind speeds compared with the model simulations and station data at KAUST for individual months from different seasons chosen to represent the four seasons. The profiles are in good agreement, although the model slightly overestimates the wind speed magnitudes. Nevertheless, the model captures the seasonal variation of wind speed well. These results indicate that our high-resolution simulations effectively reproduce local features of wind circulations.

https://doi.org/10.5194/acp-2020-444
Preprint. Discussion started: 8 July 2020


Atmospheric Chemistry and Physics
Discussions

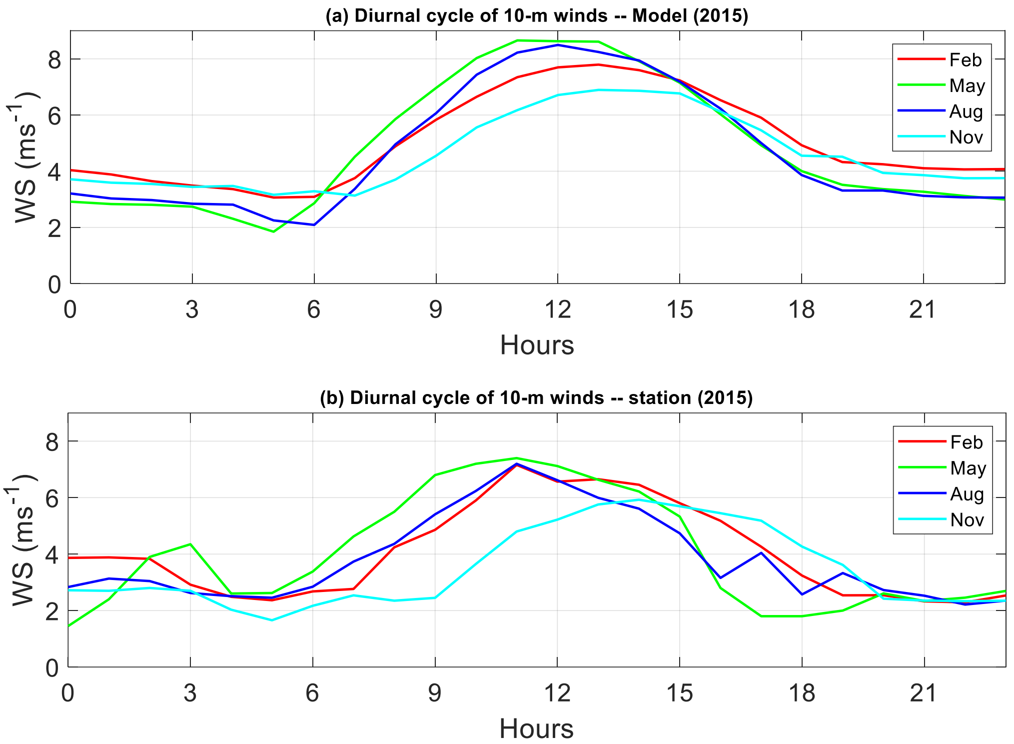


Figure 11. (a) Diurnal cycle climatology (2015) of 10-m winds at KAUST for four different months representing each season from (a) model and (b) station. Times are reported in UTC.

Figure 12 shows the diurnal cycles of aerosol extinction in KAUST–MPL data across the entire atmospheric column. Note that there are some gaps in the KAUST–MPL data because of the quality controls applied. In summer, there is significant dust activity in the morning (~ 06:00 local time), and in spring, dust activity peaks throughout the afternoon. In winter, The KAUST–MPL shows more vigorous dust activity in the nighttime (21:00 to 00:00 local time) near the surface. This increased dust activity at night is due to the effect of land breezes, which are strongest in winter (Fig. 6). We explore the effect of breezes on dust emissions and transport in section 3.4. KAUST–MPL shows high extinctions at a height of 6–7 km in summer, which represent long-range transported dust during large-scale dust events. Such high-intensity dust events are more frequent in summer and fall, as seen in the KAUST–MPL data (Fig. 7).

https://doi.org/10.5194/acp-2020-444
Preprint. Discussion started: 8 July 2020




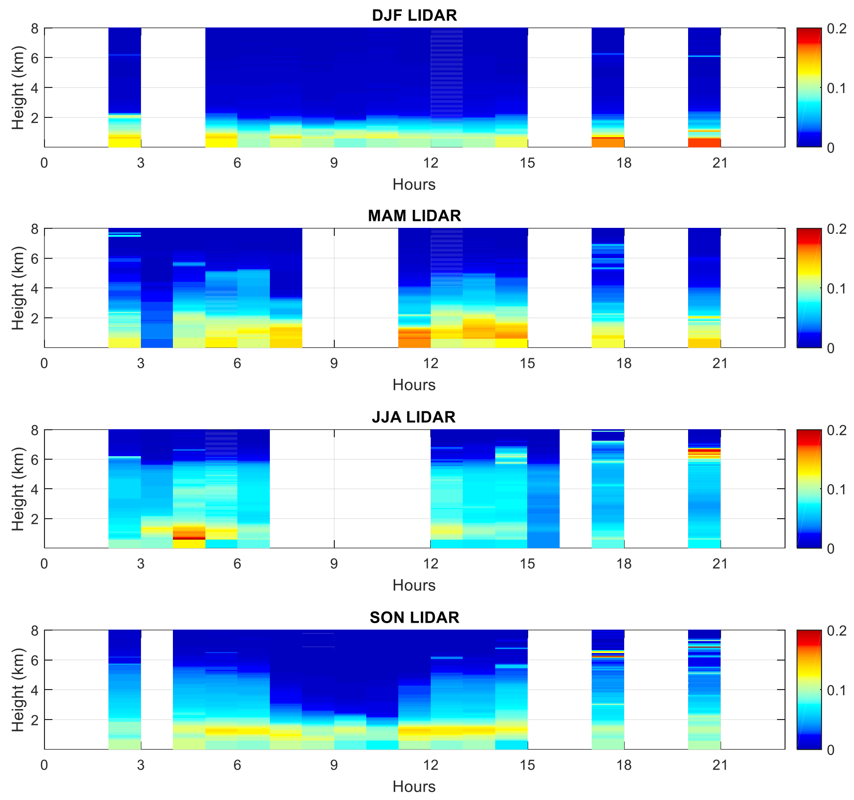


Figure 12. Diurnal profile of aerosol extinction coefficient 532nm over the atmospheric column observed by the KAUST–MPL at KAUST. Times are reported in UTC.

### 3.4. Interaction of dust aerosols with Land/sea breezes

Figure 13 shows the synoptic features of land and sea breezes in the vicinity of the KAUST–MPL site. The base map in the figure shows the high-resolution dust source function used in this study, where red hotspots represent the most dominant dust sources. Significant dust sources are observed on both sides of the Sarawat Mountain range, i.e., the coastal sides and the eastern slopes. Sea breezes are strongest in spring and summer. In contrast, land breezes are strongest in winter and fall. In the daytime, sea breezes penetrate further inland, and the KAUST–MPL site receives northwesterly winds. At night, the KAUST–MPL site experiences northeasterly land breezes, which are strongest in winter.

https://doi.org/10.5194/acp-2020-444
Preprint. Discussion started: 8 July 2020

Atmospheric Chemistry and Physics
Discussions

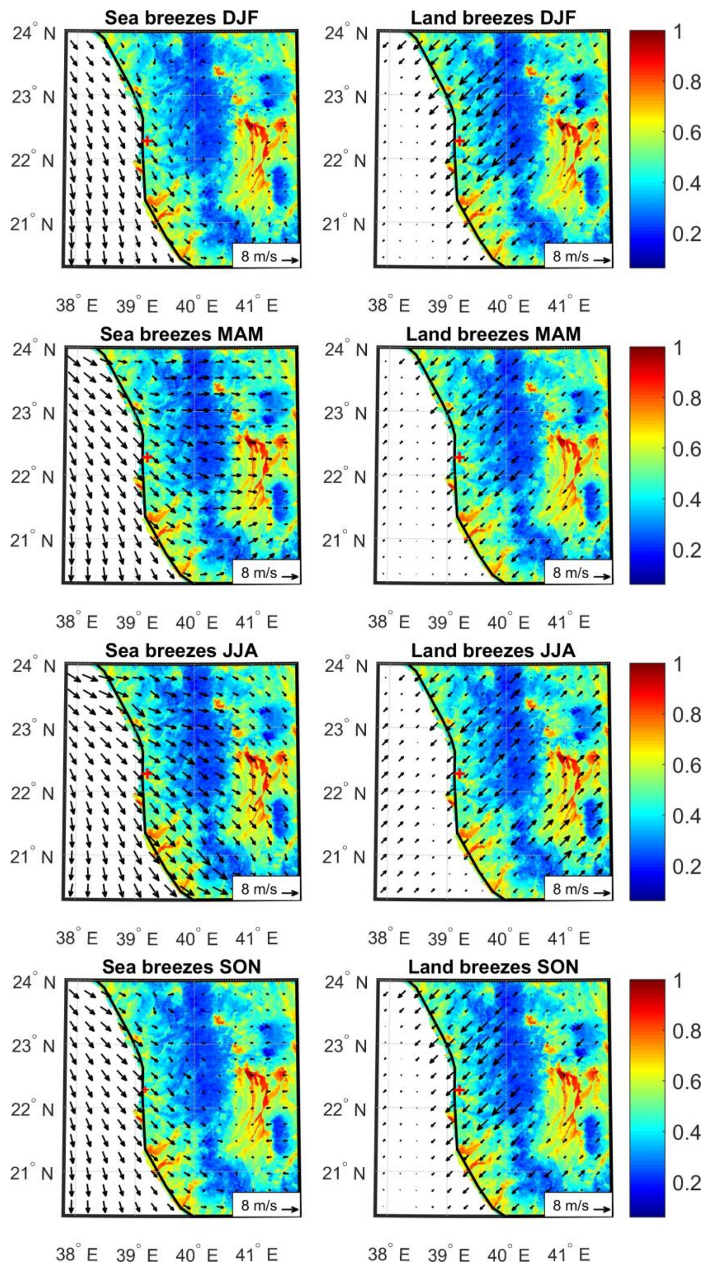


Figure 13. Model 10-m wind speed showing the land (right) and sea (left) breezes. The data are averaged during the peaks of land and sea breezes to highlight their patterns, i.e., 01:00 to 03:00 hours UTC for land breezes (night) and 14:00 to 16:00 hours UTC for sea breezes (day). KAUST site is marked by a red (+) mark. The base map shows the high-resolution dust source function (Parajuli and Zender, 2017) used in this study, in which the values range from zero to one with the highest value representing the most significant dust source region.

https://doi.org/10.5194/acp-2020-444
Preprint. Discussion started: 8 July 2020



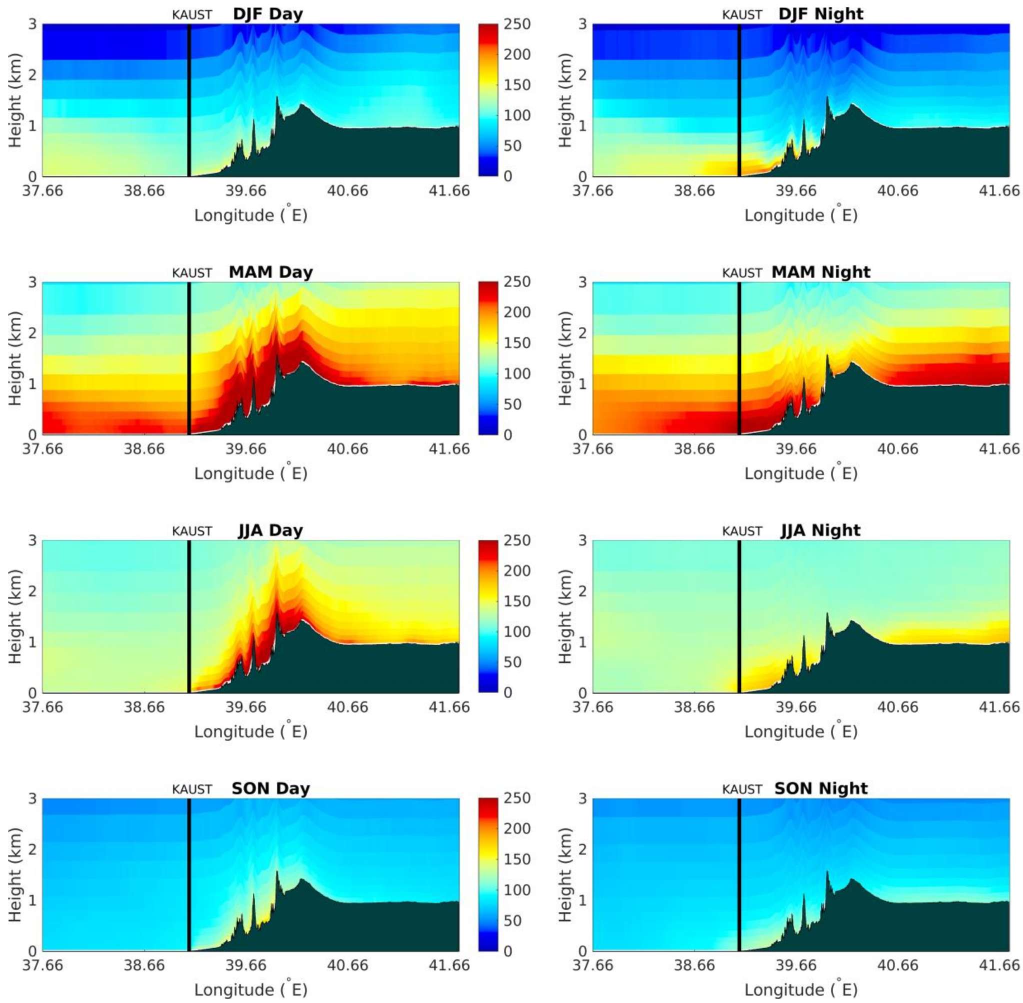


Figure 14. Longitudinal cross-section, perpendicular to the coastline, of aerosol concentrations ($\mu g\ m^{-3}$) over KAUST. Data are averaged seasonally and presented separately for day (left column) and night (right column). Data averaged during the same period as in Fig. 13 to demonstrate the effect of land and sea breezes on dust aerosols. The vertical line in black shows the location of the KAUST site. The land profile along the same section is depicted in black shades, the top of which shows the actual land elevation.

Figure 14 shows the total aerosol concentration ($\mu g\ m^{-3}$) within the innermost model domain (d03) in a longitudinal cross-section perpendicular to the coastline over KAUST. The section also shows the land profile (black shades) where the Sarawat Mountains that run along the eastern coast of the Red Sea and the relatively flat inland deserts that lie on the eastern side of the mountains are visible. The mountains reach a maximum elevation of ~1.5 km above sea level. The effect of land and sea breezes on dust is apparent in Fig. 14, as discussed in further detail below.

https://doi.org/10.5194/acp-2020-444
Preprint. Discussion started: 8 July 2020


During winter nights, a thin layer of dust collects over the marine boundary layer and the land near the KAUST site within ~1 km height. This layer of dust is an accumulation of dust that has been mobilized by land breezes from the coastal plains and the western flanks of the mountains. The coastal plains of the Red Sea are rich in fine fluvial sediments deposited by wadis, which are known sources of dust (Anisimov et al., 2017; Parajuli et al., 2019). The western flanks of the mountains also contain fluvial and intermountain deposits along the slope that are suitable for resuspension (Parajuli et al., 2014). This mobilized dust is transported towards the Red Sea, which seems to occur at low altitudes ~500 m (Fig. 14). Some dust collects over the Red Sea during the daytime in the winter also, which appears well mixed. During the day, the northwesterly sea breezes move landward because of which the dust emitted from the coastal region cannot move over the sea. Therefore, this dust observed during the daytime must be the residual dust that accumulated overnight. The dust mobilization from the coastal area by the sea breezes (daytime) is weaker during the winter.

In the spring, there is very high dust loading over the coastal region and the western flanks of the mountains, which is much higher than in winter. This higher dust loading is consistent with stronger sea breezes in spring than in winter (Fig. 13). The highest dust loading is observed over the slopes of the mountains at a height of 1–1.5 km. Recall that the LIDAR data shows a high dust loading at ~1–1.5 km height at the KAUST site. Two factors appear to contribute to this high dust loading. First, daytime sea breezes mobilize dust locally from the coastal plains and the western flanks of the mountains. These sea breezes then push the dust inland and upwards along the slope of the mountains, up to 3 km height. At the same time, the northeasterly Harmattan winds also bring dust from the nearby inland deserts towards the mountains. This dust is further uplifted when the dust-laden Harmattan winds encounter the sea breezes coming from the opposite direction. Thus, the interaction of sea breezes with the northeasterly Harmattan winds across the mountains mainly determines the vertical distribution of aerosols over the region. At night, the sea breezes weaken, and the vertical extent of dust in the atmosphere reduces. However, the atmosphere over the deserts on the eastern side of the mountains also looks remarkably dusty. This is because the land breezes become stronger at night and mobilizes dust from the deserts. The land breezes also appear to transport the dust towards the Red Sea from the western flanks of the mountains at night.

In summer, the patterns of dust mobilization and transport are similar to those in spring but are not quite as pronounced. In fall, the mobilization of dust from the coast and its ocean-ward transport is very weak, and their patterns are similar to those in winter.

The model-simulated vertical distributions of aerosols do not exactly match the KAUST–MPL profiles presented earlier (Fig. 8). Although it is difficult to identify the exact reason for this discrepancy, there are several possible explanations. Although the effect of orography on dust seems to be correctly resolved (Fig. 14), the transport of dust towards the KAUST site may not be fully resolved. Part of this discrepancy could also be because of the coarser model resolution compared to KAUST–MPL data. KAUST–MPL data is a point measurement and the model data represents the profiles at a 1.3x1.3 km grid cell, which, although high-resolution, can still produce a large difference, especially in a land-ocean boundary.

https://doi.org/10.5194/acp-2020-444
Preprint. Discussion started: 8 July 2020


Atmospheric Chemistry and Physics Discussions

Figure 15 shows the daytime and nighttime winds at three altitudes for two specific months in summer (August) and winter (February). Note that the winds are shown at different levels for August and February to highlight the features of land and sea breezes better. The depth of sea breezes and land breezes are different, as expected, with the sea breezes being much deeper than the land breezes, primarily because the PBL is higher during the day than at night. The local topography also plays a role. Sea breezes are still strong up to a height of ~1150m; however, the land breezes only reach a height of ~200m. By about 450m, the land breezes subside completely. The land breeze circulation is confined by the height of the mountains, whereas the sea breeze circulation extends to a much higher altitude. The returning flow of the sea breezes takes place at a height of ~2250m in the form of northeasterly trade winds, which are responsible for bringing the dust to our site from the inland deserts. The return flow of the land breezes occurs at a height of ~1500m with a change of direction of nearly $180^{o}$ of the lower part of the subtropical westerly jets (de Vries et al., 2013) (see supporting information Fig. S6). The variation in the pattern of these winds along the vertical dimension is generally consistent with the profile of modeled dust that we presented earlier (Fig. 14).

In summary, the timings and patterns of dust emission and transport in the study region are evidently affected by land and sea breezes. These results are summarized in the schematic diagram in Fig. 1. Note that, across the majority of the Arabian Peninsula, the seasonality of dust mobilization is quite different to our study region, where dust emission and transport are maximum during summer (Parajuli et al., 2019).

Atmospheric Chemistry and Physics
Open Access
Discussions

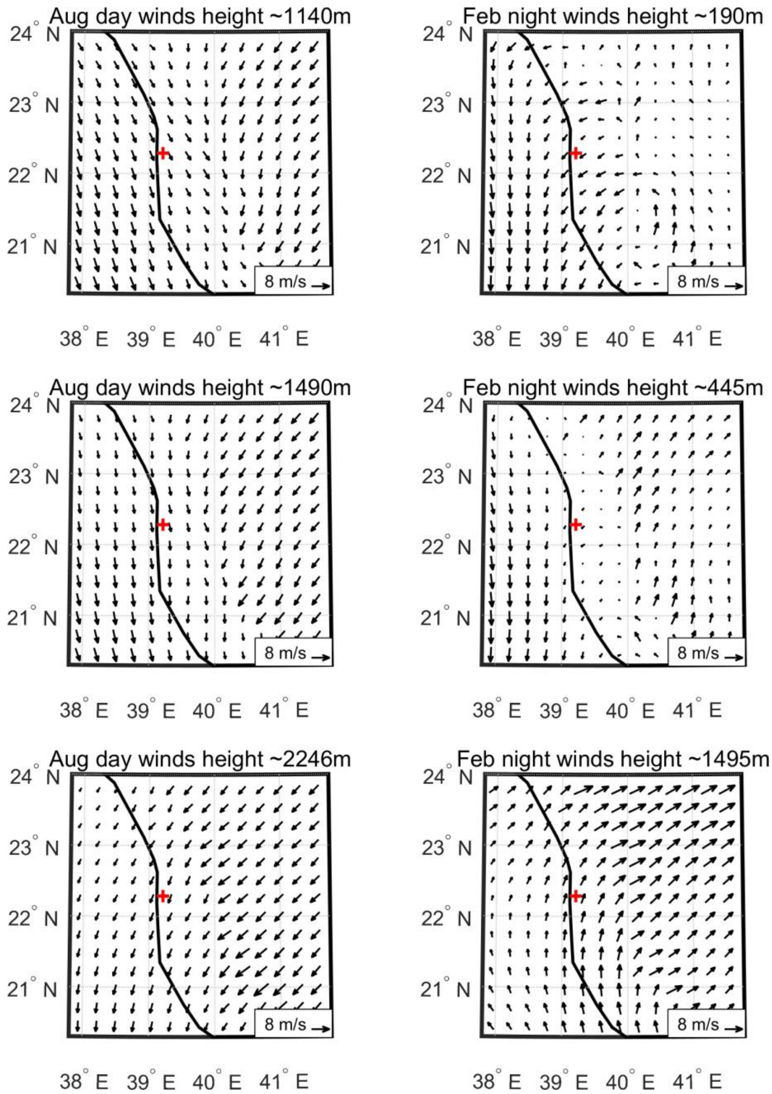


Figure 15. Model (WRF) winds at three different elevations for August (left) and February (right) within the study domain. The KAUST site is marked by a red (+) symbol.

https://doi.org/10.5194/acp-2020-444
Preprint. Discussion started: 8 July 2020


Atmospheric Chemistry and Physics Discussions
Open Access
EGU

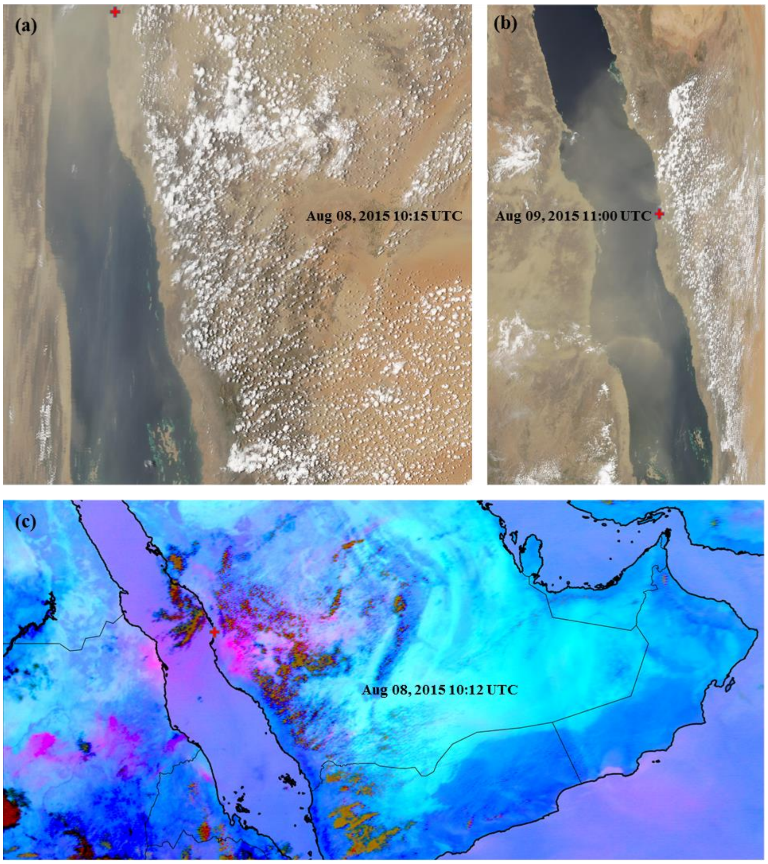


Figure 16. MODIS and SEVIRI images during a large-scale dust event. True color images from MODIS on (a) August 08, 2015 10:15 UTC (b) August 09, 2015 11:00 UTC, and (c) Meteosat SEVIRI RGB dust composite for Aug 08, 2015 10:12 UTC. KAUST site is marked by a red (+) symbol.

### 3.5. Case study of a summer-time dust event

A large-scale dust storm swept over the KAUST site on August 08, 2015, as seen in the MODIS image in Fig. 16a. The dust event lasted for two days until August 09. The KAUST AERONET station registered the second-highest AOD of the entire year on August 08 with the daily mean AOD reaching 2.48. The AERONET angstrom exponent (AE 440/675) value showed a sharp reduction on this day, from 0.41 on August 06 to 0.10 on August 08. This reduction indicates the dominance of coarse-mode dust during the event and thus, that the dust event originated from nearby inland deserts. By August 09, the dust storm moved towards the south/southwest and spread to a broader region across the Red Sea and northeast Africa. The MODIS RGB image on August 09 shows a dust plume originating from northeast Africa around Port Sudan, which, after being deflected by the northerly winds, experiences a marked curvature (Fig. 16b).

https://doi.org/10.5194/acp-2020-444
Preprint. Discussion started: 8 July 2020



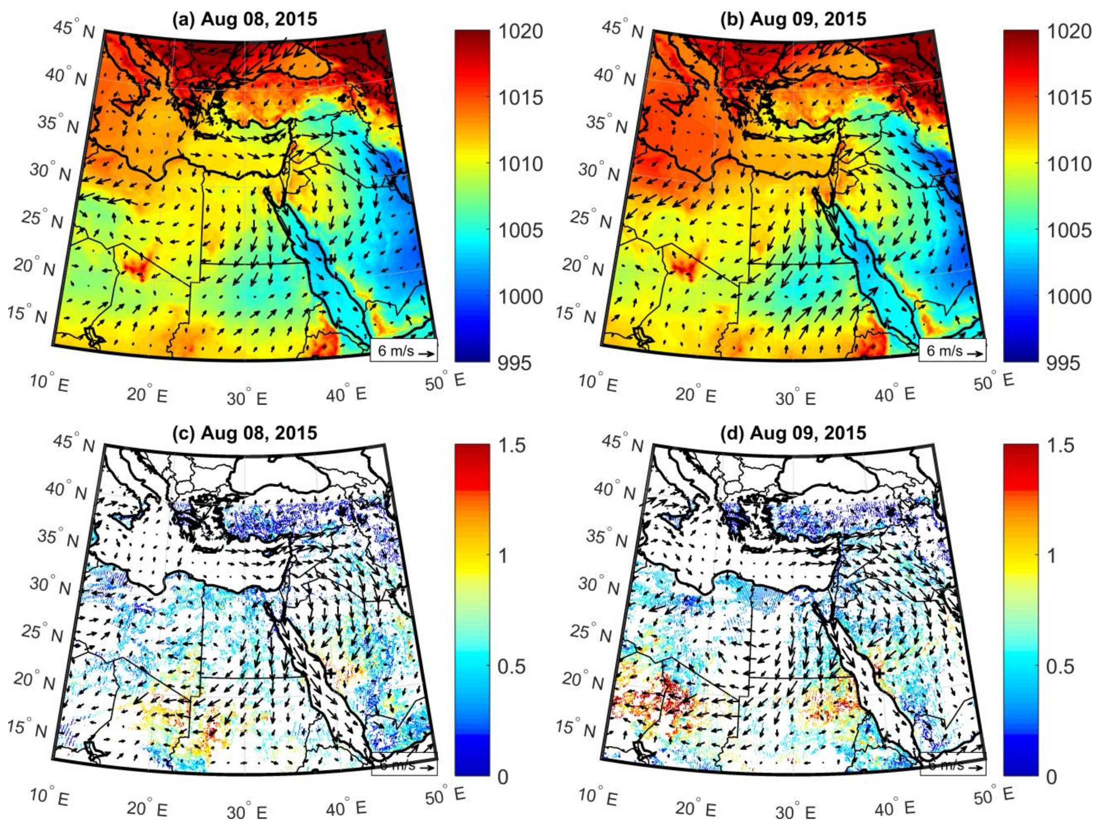


Figure 17. Surface pressure and wind vectors from ECMWF operational analysis data during the dust event (a and b), and MODIS deep blue AOD data overlain by model wind vectors (c and d).

The synoptic conditions of this dust event are somewhat similar to those of a summer-time dust event reported by Kalenderski and Stenchikov (2016), which was centered over North Sudan. The dust event we describe here is a typical summer-time dust event caused by high winds driven by strong pressure gradients (Alharbi et al., 2013). Although haboob-type dust events commonly occur in the region, analysis of the RGB pink dust composite (Fig. 16c) shows only a few scattered clouds over the study site during this period, ruling out the possibility of a haboob dust event. Haboob is a typical dust event that commonly occurs in regions with moisture convection, in which dust is generated by strong divergent winds that form around a cold pool of downdrafts (Anisimov et al., 2018).

As seen in Figs. 17a, b, a high-pressure system developed in the eastern Mediterranean region and Turkey on August 08, which expanded towards Africa/Middle East and created stronger winds over the region on August 09. On August 08, a low-pressure system developed, which was centered around northeast Africa (Sudan). Winds converging towards this low from the north/northeast adopted a northeasterly flow pattern, which is characteristic of the Harmattan winds prevalent in the region. The winds originating from the eastern Mediterranean were forced to curve by the Hijaz mountains in the western Arabian Peninsula, finally converging with the low-pressure system in northeast Africa and the Red Sea, where the high energy of the flow was finally dissipated. A high-pressure system persisted throughout the dust event over the Ethiopian highlands and south Sudan, as shown in Figs. 16a, b. This high-pressure system gave rise to the southerly/southwesterly winds that also converged towards the low-pressure region around northeast Africa and the Red Sea.

MODIS AOD also showed a high aerosol loading around KAUST (+ symbol in Figs. 17c, d) on August 08 that spread across a larger area towards northeast Africa on August 09. Figure 17 shows that the dust mobilization was evidently caused by the northerly/northeasterly winds moving over the study site. The wind vector patterns are very consistent between ECMWF operational analysis (Figs. 17a, b) and model simulations (Figs. 17c, d) for most parts of the domain. This observation is not surprising because we use the ECMWF operational analysis data for boundary conditions and apply 'grid nudging' at each model grid using the same ECMWF dataset. The wind patterns in the two figures differ in some areas, however, especially over the Ethiopian highlands. Note that the model winds presented are derived from the coarser 12 km domain to show the wind patterns over a larger region beyond our innermost study domain. In the Ethiopian highlands region, where there is a strong effect from the topography, such a coarse resolution may not be enough to resolve the fine features of the wind circulations. At the study site, however, winds are indeed better resolved in our model because the resolution of the innermost domain is much higher, i.e., 1.33 km.

The model captures the major features of the dust storm reasonably well. Both the model and the AERONET data register this event as the second-largest dust event of 2015. On August 09, the model shows a daily average (daytime only) AOD of 1.18 compared to 1.79 given by the AERONET data (underestimation by ~35 %).

Figure 18 compares the vertical profiles of dust as provided by model simulations and the KAUST–MPL data during the dust event. The right column in the figure shows the simulated dust extinction coefficient at 550nm, covering the three days during the dust event. Because of the quality constraints applied, the processed extinction data from KAUST–MPL are only partially available during this event. Therefore, we present the raw normalized relative backscattering (NRB) from the KAUST–MPL to examine the evolution of this dust event qualitatively, as shown in Fig. 18. Note that around noon local time in summer, the KAUST–MPL field of view is covered to avoid the sun glare, which is why there is some gap in the data around this time. In the KAUST–MPL NRB data (Fig. 18, left column), the dust plume appears as early as Aug 08 (~05:00 UTC) at a height of 1–1.5 km, indicating the onset of the dust storm. This dust plume becomes strongest by August 09, covering a large part of the atmospheric column with dust. Although the onset of the dust event is slightly earlier in the model compared to KAUST–MPL data, the model also shows high dust activity on August 09, consistent with KAUST–MPL observations. The dust is mainly confined within a height of ~2 km, which is consistent in both datasets. We also observed a higher intrusion of dust into the atmosphere, which is expected because the PBL is well developed in summer.

Note that the model data also show a high extinction at a height of ~6 km on August 09/10, particularly at night (Fig. 18), which is consistent with the dust layers observed at 6–7 km height

https://doi.org/10.5194/acp-2020-444
Preprint. Discussion started: 8 July 2020



in the KAUST–MPL nighttime data (Fig. 8). Although the model data does not identify these dust layers at 6–7 km in the seasonally averaged profiles presented earlier (Fig. 8), the model nonetheless correctly identified these same dust layers in this event (Fig. 18). The demise timing of the dust storm is consistent in both the model and KAUST–MPL data. These results further confirm that the dust layers observed at 6–7 km height correspond to the long-range transported dust during large-scale dust events.

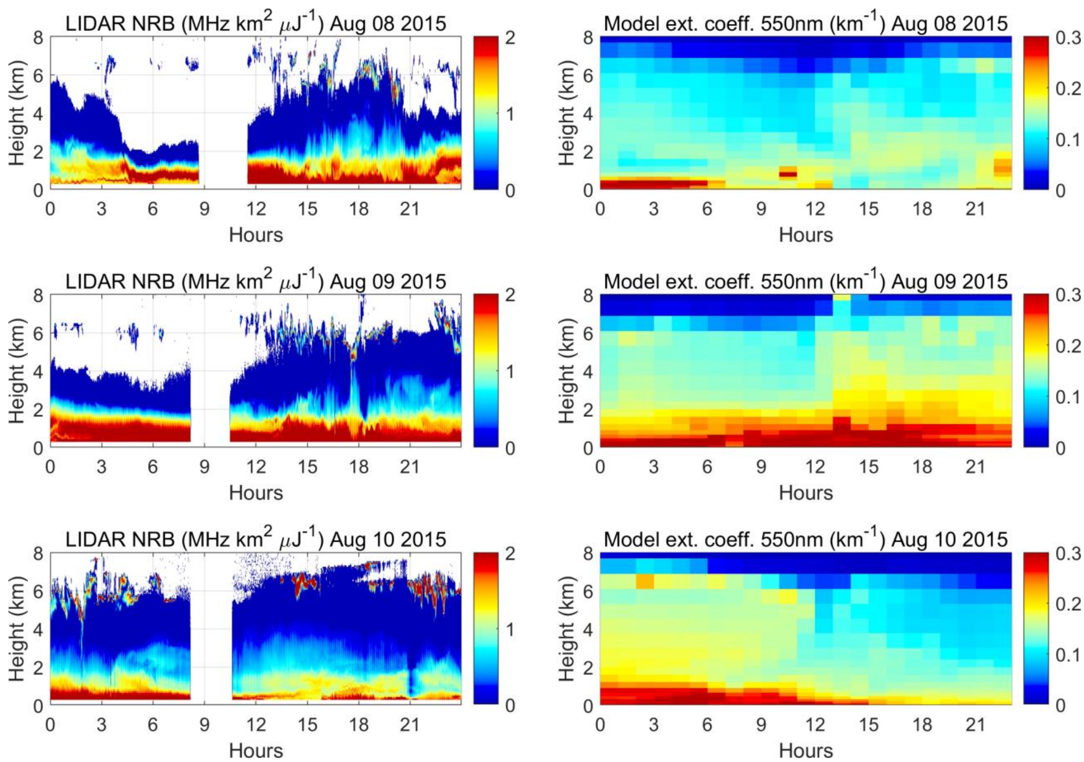


Figure 18. Natural logarithm of normalized relative backscatter (NRB) at 532 nm measured at the KAUST–MPLNET station (left column) and the model-simulated dust extinction coefficient at 550 nm (right column) during the dust event of August 08/09. Times are reported in UTC.

## 4. Discussion and conclusion

In this study, we investigated three main aspects of dust aerosols over the eastern coast of the Red Sea. We used data collected from the only operating LIDAR in the region, located on the KAUST campus, together with other collocated observations and high-resolution WRF-Chem model simulations. To summarize, we first investigated the vertical profile of aerosol extinction and concentrations, as well as their seasonal and diurnal variability over the study site. Secondly, we evaluated how accurately WRF-Chem reproduced the vertical profiles of aerosols over the study site and examined its performance during a large-scale dust event of 2015. Thirdly, we investigated how the prevailing land and sea breezes affected the distribution of dust over the site, which is located exactly at the land-ocean boundary. This study represents a first attempt to

https://doi.org/10.5194/acp-2020-444
Preprint. Discussion started: 8 July 2020




understand and describe the interactions between breezes and dust in this largely understudied region. The main findings of this research are summarized as follows.

- The simulated AOD obtained from the high-resolution WRF-Chem model setting is reasonably consistent over the study site across all observational datasets, including AERONET, MODIS, and MISR. The simulated AOD shows a mean bias error (MBE) of ~13.4 % with the AERONET data.
- WRF-Chem simulations show that dust has the highest contribution to total AOD among all aerosol types, contributing up to 92 % in summer. Anthropogenic (sulfate, OC, and BC) and sea salt aerosols contribute up to 15 % and 6 % to the total AOD, respectively, both of which are highest in winter.
- Over the study site, most dust is confined in the troposphere, within a height of 8 km. In winter, dust is confined to lower altitudes than in summer, which is consistent with the lower PBL height in winter than in summer.
- There is a marked difference in the daytime and nighttime vertical profile of aerosols in the study site, as shown by the KAUST–MPL data. We observed a prominent dust layer at ~5–7 km in the nighttime in the KAUST–MPL data, which is supposedly formed by dust lifted up by day-time convection in the central-peninsula deserts and transported to the coast by easterly winds.
- The climatology of the vertical profile of daytime dust extinction is consistent in the KAUST–MPL, MERRA-2, and CALIOP data in all seasons, which is well reproduced by our WRF-Chem simulations. The profiles from the different datasets match better in winter than in summer, which is consistent with the results of Wu et al. (2017).
- There is significant diurnal variation in aerosol loading at the study site in all seasons, as shown by the KAUST–MPL data. Stronger aerosol activity occurs in the early morning during the summer, in the afternoon during the spring, and in the night during the winter.
- Both sea and land breezes in daytime and nighttime, respectively, create dust emissions from the coastal plains and the western flanks of the Sarawat Mountains. Such dust emissions are most prevalent in spring.
- The nighttime land breezes are strongest in winter; these northeasterly land breezes transport dust aerosols from the coastal plains and the mountain slopes towards the Red Sea. The sea breeze circulation is much deeper (~2 km) than the land breeze circulation (~1 km), as illustrated in Fig. 1.
- Sea breezes push the dust mobilized from the coastal plains up along the slope of the Sarawat Mountains, which subsequently encounters the dust-laden northeasterly trade winds coming from inland deserts, causing elevated dust maxima at a height of ~1.5 km above sea level across the mountains.
- WRF-Chem qualitatively captured the evolution of a large-scale summertime dust event in 2015 over the study site. The model simulated the onset, demise, and the height of the dust storms reasonably well.

The seasonal climatology of aerosol vertical profiles was consistent among all datasets that we compared, viz. KAUST–MPL, MERRA-2, and CALIOP, despite their different vertical and

https://doi.org/10.5194/acp-2020-444
Preprint. Discussion started: 8 July 2020

Atmospheric Chemistry and Physics Discussions

horizontal resolutions. These seasonal profiles were consistent with those reported by Li et al. (2018) over the same region. The WRF-Chem model successfully reproduced the vertical profiles of dust aerosol extinction and concentration in terms of seasonal climatology, when compared with the abovementioned datasets. Nearer the surface, the model showed some disagreement with the observational datasets, as also noted in some previous studies (e.g., Hu et al., 2016; Wu et al., 2017; Flaounas et al., 2017). Note that such disagreement between data collected near the surface exists among the observational datasets as well; this disagreement arises due to differences in the retrieval algorithms used as well as differences in the resolution of the datasets.

Analysis of the KAUST–MPL data revealed several interesting features of the vertical profile of aerosols over the study site, which had not been previously documented in other studies. For example, we observed a significant difference between the daytime and nighttime vertical profiles of aerosols. Some of these detailed features were not apparent in the model simulations. The model underestimated the nighttime aerosol extinctions at 5–7 km height in summer and fall compared to the KAUST–MPL data, which we attributed to the model's inability to represent either the deep convective mixing of dust in the central-peninsula deserts and/or long-range transport of aerosols to the coastal regions.

Both KAUST–MPL and the model data identified two prominent layers of dust over the study site, one at a lower altitude (~1–2 km) and another at higher altitude (~6–7 km). These two dust layers corresponded to two different dust sources. The lower dust layer corresponded to dust originating from nearby deserts, and the upper dust layer corresponded to dust coming from more remote sources and further inland. The two layers of dust are typical in this region during a large-scale dust event. As explained before, a large-scale disturbance usually brings dust from remote sources at higher altitudes (~6–7 km). When the disturbance comes closer to the site, high surface winds associated with the disturbance also pick up more dust from nearby deserts giving rise to a high dust loading at ~1–2 km height. It is obvious that the upper layer of dust consist of finer particles and the lower layer of coarser particles.

The aerosol extinction profiles observed in our study site may be broadly representative of typical aerosol profiles near other land-ocean boundaries. However, as demonstrated by our results, vertical profiles of aerosols can be affected by local or regional processes, which indicate that the profiles can differ across different regions. Therefore, it is vital to examine the aerosol vertical profiles of a region to understand the regional climate.

KAUST–MPL-retrieved aerosol vertical profiles also provided an opportunity to understand how aerosols interact with land and sea breezes over the eastern coast of the Red Sea, as summarized in Fig. 1. Such fine-level interactions are often poorly resolved in coarse-scale simulations. Our high-resolution simulations (~1.33x1.33 km) nonetheless correctly resolved these features and showed how breezes affect dust aerosol distribution over the region. Our study is important because the breezes and dust can directly affect the daily life of populations that reside in the coastal area. Furthermore, dust over the region affects the surface temperature of the Red Sea through changes in radiation (Sokolik and Toon, 1998; Osipov et al., 2015, Osipov et al., 2018).

Additionally, changes in dust deposition also affect the availability of nutrients delivered to marine ecosystems (Prakash et al., 2015).

The model successfully captured the evolution of a dust event that occurred in 2015 over the study site in terms of its onset and demise, as well as the height of the dust layer. Our results were consistent with several previous studies, such as Yuan et al. (2019) and Anisimov et al. (2018). However, the model underestimated the AOD at KAUST by about 35 % during the event compared to AERONET AOD. Simulating these complex, large-scale dust events is extremely challenging, and thus, we do not expect the model to capture them as precisely, since they occur only a few times (~2-3) in a year. Despite this discrepancy, the average climatological vertical profiles of aerosol concentrations and temporal variations of AODs simulated by the WRF-Chem model were broadly consistent with the observations (Figs. 3, 7, 8, 10). We note that the performance of WRF-Chem to simulate these large-scale dust events is case-specific (e.g., Teixeira et al., 2016; Fernández et al., 2019) and should not be generalized. The model performance was indeed sensitive to the type of dust event (e.g., Kim et al., 2017), the details of the dust-emission processes (Klose and Shao, 2012; Klose and Shao, 2013), the dust source function used (Kalenderski and Stenchikov 2016; Parajuli et al., 2019), and the prescribed size distribution of the emitted dust (Kok et al., 2017; Marenco et al. 2018).

MPL data are invaluable for studying the vertical details of aerosols in the atmosphere because they measure backscatter from aerosols and clouds with a high vertical and temporal resolution. Most satellite data only provide aerosol properties over the entire atmospheric column, which are complemented by the MPL data that provides height, depth, and the particle characteristics of the aerosol layers in the atmosphere. Since satellite data usually have low temporal resolution, and because many large-scale dust events are short-lived, MPL data can reveal additional characteristics of dust storms.

In regional and global climate models, it is a usual practice to constrain the total AOD using some observations (e.g., Zhao et al., 2010; Parajuli et al., 2019). While such constraints are desirable because they help to represent columnar atmospheric properties more precisely, they are not sufficient for certain applications such as air quality modeling, for example (Ukhov et al., 2020). Unless the model correctly represents the aerosol vertical profiles, the model-estimated surface aerosol concentrations may not be reliable. In this context, KAUST–MPL data can be instrumental in constraining the vertical distribution of aerosols in the models. Such constraints would ideally benefit the operational forecasting of dust storms and air quality (Zhang et al., 2015).

Although derived from actual observations, KAUST–MPL retrievals are also subject to uncertainties, and their accuracy is dependent on assumptions made by the retrieval algorithms. A study that compared the GRASP retrieval scheme employed here against in situ measurements showed that the differences were less than 30 % for the different retrieval schemes (Benavent-Oltra et al., 2019).

*Codes and data availability.* Calibrated MPL data used in this study can be obtained from the MPLNET website https://mplnet.gsfc.nasa.gov/. The source code and additional information about the GRASP algorithm can be obtained from the grasp-open web site https://www.grasp-open.com/. MODIS AOD data were downloaded from http://ladsweb.nascom.nasa.gov/data/. MERRA-2 data were obtained from the NASA Goddard Earth Sciences Data and Information Services Center (GES DISC) available at https://disc.sci.gsfc.nasa.gov/daac-bin/FTPSubset2.pl. CALIOP data were retrieved from the website of Atmospheric Science Data Center, NASA Langley Research Center, available at https://eosweb.larc.nasa.gov/project/calipso/cloud-free_aerosol_L3_LIDAR_table. ECMWF Operational Analysis data are restricted data, which were retrieved from http://apps.ecmwf.int/archive-catalogue/?type=4v&class=od&stream=oper&expver=1 with a membership. EDGAR-4.2 is available at http://edgar.jrc.ec.europa.eu/overview.php?v=42. OMI-HTAP data are available at https://avdc.gsfc.nasa.gov/pub/data/project/OMI_HTAP_emis. A copy of the input datasets and details of the WRF-Chem model configuration can be downloaded from the KAUST repository http://hdl.handle.net/10754/662750 or by e-mail request to psagar@utexas.edu.

*Acknowledgements.* The research reported in this publication was supported by funding from King Abdullah University of Science and Technology (KAUST). We thank the KAUST Supercomputing Laboratory for providing computing resources. We also thank Anatolii Anisimov for providing SEVIRI images and for helpful discussions. We are grateful to Ellsworth Judd Welton of NASA Goddard Space Flight Center for the help in archiving and processing the raw LIDAR data. Thanks are also due to Michael Cusack of KAUST for proofreading the manuscript.

*Author contributions.* SPP and GLS developed the main scientific concept of the paper. SPP analyzed the data and wrote the paper with inputs from GLS. IS operated and maintained the KAUST–MPL site. SPP conducted WRF-Chem simulations and AU contributed on code modifications. OD and AL ran the GRASP code. GLS conceived, designed, and oversaw the study. All authors discussed the results and contributed to the final manuscript.

*Competing interests.* The authors declare that they have no conflict of interest.

https://doi.org/10.5194/acp-2020-444
Preprint. Discussion started: 8 July 2020


Atmospheric Chemistry and Physics Discussions
Open Access

## References

Ackerman, S. A.: Remote Sensing Aerosols Using Satellite Infrared observations, J. Geophys. Res., 102, 17069–17079, https://doi.org/10.1029/96JD03066, 1997.

Albugami S., Palmer S., Cinnamon J., and Meersmans J.: Spatial and Temporal Variations in the Incidence of Dust Storms in Saudi Arabia Revealed from In Situ Observations, Geosciences, 9, 162, https://doi.org/10.3390/geosciences9040162, 2019.

Alharbi, B. H., Maghrabi, A. L., and Tapper, N.: The March 2009 dust event in Saudi Arabia: Precursor and supportive environment, B. Am. Meteorol. Soc., 94, 515-528, https://doi.org/10.1175/BAMS-D-11-00118.1, 2013.

Almazroui, M., Raju, P.V.S., Yusef, A., Hussein, M. A. A., and Omar, M.: Simulation of extreme rainfall event of November 2009 over Jeddah, Saudi Arabia: the explicit role of topography and surface heating, Theor. Appl. Climatol., 132**,** 89–101, https://doi.org/10.1007/s00704-017-2080-2, 2018.

Anisimov, A., Tao, W., Stenchikov, G., Kalenderski, S., Prakash, P. J., Yang, Z.-L., and Shi, M.: Quantifying local-scale dust emission from the Arabian Red Sea coastal plain, Atmos. Chem. Phys., 17, 993–1015, https://doi.org/10.5194/acp-17-993-2017, 2017.

Barnard, J. C., Fast, J. D., Paredes-Miranda, G., Arnott, W. P., and Laskin, A.: Technical Note: Evaluation of the WRF-Chem "Aerosol Chemical to Aerosol Optical Properties" Module using data from the MILAGRO campaign, Atmos. Chem. Phys., 10, 7325–7340, https://doi.org/10.5194/acp-10-7325-2010, 2010.

Bangalath, H. K., and Stenchikov, G.: Role of dust direct radiative effect on the tropical rain belt over Middle East and North Africa: A high- resolution AGCM study, J. Geophys. Res. Atmos., 120, 4564–4584, https://doi.org/10.1002/2015JD023122, 2015.

Benavent-Oltra, J. A., Román, R., Casquero-Vera, J. A., Pérez-Ramírez, D., Lyamani, H., Ortiz-Amezcua, P., Bedoya-Velásquez, A. E., de Arruda Moreira, G., Barreto, Á., Lopatin, A., Fuertes, D., Herrera, M., Torres, B., Dubovik, O., Guerrero-Rascado, J. L., Goloub, P., Olmo-Reyes, F. J., and Alados-Arboledas, L.: Different strategies to retrieve aerosol properties at night-time with the GRASP algorithm, Atmos. Chem. Phys., 19, 14149–14171, https://doi.org/10.5194/acp-19-14149–2019, 2019.

Chapman, E. G., Gustafson Jr, W. I., Easter, R. C., Barnard, J. C., Ghan, S. J., Pekour, M. S., and Fast, J. D.: Coupling aerosol-cloud-radiative processes in the WRF-Chem model: Investigating the radiative impact of elevated point sources, Atmos. Chem. Phys., 9, 945–964, https://doi.org/10.5194/acp-9-945-2009, 2009.

Chin, M., Ginoux, P., Kinne, S., Torres, O., Holben, B.N., Duncan, B.N., Martin, R.V., Logan, J.A., Higurashi, A. and Nakajima, T.: Tropospheric aerosol optical thickness from the GOCART model and comparisons with satellite and Sun photometer measurements, J. Atmos. Sci., 59, 461–483, https://doi.org/10.1175/1520-0469(2002)059<0461:TAOTFT>2.0.CO;2, 2002.

Chin, M., Diehl, T., Ginoux, P., and Malm, W.: Intercontinental transport of pollution and dust aerosols: implications for regional air quality, Atmos. Chem. Phys., 7, 5501–5517, https://doi.org/10.5194/acp-7-5501-2007, 2007.

Crouvi, O., Dayan, U., Amit, R., and Enzel, Y.: An Israeli haboob: Sea breeze activating local anthropogenic dust sources in the Negev loess, Aeol. Res., 24, 39–52, https://doi.org/10.1016/j.aeolia.2016.12.002, 2017.

Davis, S. R., Farrar, J. T., Weller, R. A., Jiang, H., and Pratt, L. J.: The Land- Sea Breeze of the Red Sea: Observations, Simulations, and Relationships to Regional Moisture Transport, J. Geophys. Res. Atmos., 124, https://doi.org/10.1029/2019JD031007, 2019.

Derimian, Y., Choël, M., Rudich, Y., Deboudt, K., Dubovik, O., Laskin, A., Legrand, M., Damiri, B., Koren, I., Unga, F., Moreau, M., Andreae, M. O., and Karnieli, A.: Effect of sea breeze circulation on aerosol mixing state and radiative properties in a desert setting, Atmos. Chem. Phys., 17, 11331–11353, https://doi.org/10.5194/acp-17-11331-2017, 2017.

de Vries, A. J., Tyrlis, E., Edry, D., Krichak, S. O., Steil, B., and Lelieveld, J.: Extreme precipitation events in the Middle East: Dynamics of the Active Red Sea Trough, J. Geophys. Res. Atmos., 118, 7087– 7108, doi:10.1002/jgrd.50569, 2013.

Di Biagio, C., Formenti, P., Balkanski, Y., Caponi, L., Cazaunau, M., Pangui, E., Journet, E., Nowak, S., Caquineau, S., Andreae, M. O., Kandler, K., Saeed, T., Piketh, S., Seibert, D., Williams, E., and Doussin, J.-F.: Global scale variability of the mineral dust long-wave refractive index: a new dataset of in situ measurements for climate modeling and remote sensing, Atmos. Chem. Phys., 17, 1901-1929, https://doi.org/10.5194/acp-17-1901-2017, 2017.

Diner, D.: MISR Level 3 Component Global Aerosol product covering a day HDF-EOS File - Version 4 [Data set], NASA Langley Atmospheric Science Data Center DAAC, https://doi.org/10.5067/terra/misr/mil3dae_l3.004, 2009.

Dubovik, O., and King, M. D.: A flexible inversion algorithm for retrieval of aerosol optical properties from Sun and sky radiance measurements, J. Geophys. Res., 105, 20673– 20696, https://doi.org/10.1029/2000JD900282, 2000.

Dubovik, O., Herman, M., Holdak, A., Lapyonok, T., Tanré, D., Deuzé, J. L., Ducos, F., Sinyuk, A., and Lopatin, A.: Statistically optimized inversion algorithm for enhanced retrieval of aerosol properties from spectral multi-angle polarimetric satellite observations, Atmos. Meas. Tech., 4, 975–1018, https://doi.org/10.5194/amt-4-975-2011, 2011.

Dubovik, O., Lapyonok, T., Litvinov, P., Herman, M., Fuertes, D., Ducos, F., Lopatin A., Chaikovsky, A., Torres, B., Derimian, Y., Huang, X., Aspetsberger, M., and Federspiel, C.: GRASP: a versatile algorithm for characterizing the atmosphere, SPIE Newsroom, *25*, https://doi.org 10.1117/2.1201408.005558, 2014.

Estoque, M. A.: A theoretical investigation of the sea breeze, Q.J.R. Meteorol. Soc., 87, 136-146, https://doi.org/10.1002/qj.49708737203, 1961.

Farrar, J., Lentz, S., Churchill, J., Bouchard, P., Smith, J., Kemp, J., Lord, J., Allsup, G., and Hosom, D.: King Abdullah University of Science and Technology (KAUST) mooring deployment cruise and fieldwork report, Technical report, Woods Hole Oceanographic Institution, WHOI-KAUST-CTR-2009, 2, 2009.

Fast, J.D., Gustafson Jr, W.I., Easter, R.C., Zaveri, R.A., Barnard, J.C., Chapman, E.G., Grell, G.A., and Peckham, S.E.: Evolution of ozone, particulates, and aerosol direct forcing in an urban area using a new fully- coupled meteorology, chemistry, and aerosol model, J. Geophys. Res., 111, https://doi.org/10.1029/2005JD006721, 2006.

Fernández-Camacho, R., Rodríguez, S., de la Rosa, J., Sánchez de la Campa, A. M., Viana, M., Alastuey, A., and Querol, X.: Ultrafine particle formation in the inland sea breeze airflow in Southwest Europe, Atmos. Chem. Phys., 10, 9615–9630, https://doi.org/10.5194/acp-10-9615-2010, 2010.

Flaounas, E., Kotroni, V., Lagouvardos, K., Klose, M., Flamant, C., and Giannaros, T. M.: Sensitivity of the WRF-Chem (V3.6.1) model to different dust emission parametrisation: assessment in the broader Mediterranean region, Geosci. Model Dev., 10, 2925–2945, https://doi.org/10.5194/gmd-10-2925-2017, 2017.

Fernández, A.J., Sicard, M., Costa, M.J., Guerrero-Rascado, J.L., Gómez-Amo, J.L., Molero, F., Barragán, R., Basart, S., Bortoli, D., Bedoya-Velásquez, A.E. and Utrillas, M.P.: Extreme, wintertime Saharan dust intrusion in the Iberian Peninsula: KAUST–MPL monitoring and evaluation of dust forecast models during the February 2017 event, Atmos. Res., 223–241, https://doi.org/10.1016/j.atmosres.2019.06.007, 2019.

Ginoux, P., Chin, M., Tegen, I., Prospero, J. M., Holben, B., Dubovik, O., and Lin, S.- J.: Sources and distributions of dust aerosols simulated with the GOCART model, J. Geophys. Res., 106, 20255– 20273, doi:10.1029/2000JD000053, 2001.

Gong, S. L.: A parameterization of sea- salt aerosol source function for sub- and super- micron particles, *Global Biogeochem. Cycles*, 17, 1097, https://doi.org/10.1029/2003GB002079, 2003.

Hu, Z., Zhao, C., Huang, J., Leung, L. R., Qian, Y., Yu, H., Huang, L., and Kalashnikova, O. V.: Trans-Pacific transport and evolution of aerosols: evaluation of quasi-global WRF-Chem simulation

https://doi.org/10.5194/acp-2020-444
Preprint. Discussion started: 8 July 2020


Atmospheric Chemistry and Physics Discussions

with multiple observations, Geosci. Model Dev., 9, 1725–1746, https://doi.org/10.5194/gmd-9-1725-2016, 2016.

Hubert, W.E., Hull, A.N., Morford, D.R. and Englebretson, R.E.: Forecasters handbook for the Middle East/Arabian Sea, OCEAN DATA SYSTEMS INC MONTEREY CALIF, 1983.

Janssens-Maenhout, G., Crippa, M., Guizzardi, D., Dentener, F., Muntean, M., Pouliot, G., Keating, T., Zhang, Q., Kurokawa, J., Wankmüller, R., Denier van der Gon, H., Kuenen, J. J. P., Klimont, Z., Frost, G., Darras, S., Koffi, B., and Li, M.: HTAP_v2.2: a mosaic of regional and global emission grid maps for 2008 and 2010 to study hemispheric transport of air pollution, Atmos. Chem. Phys., 15, 11411–11432, https://doi.org/10.5194/acp-15-11411-2015, 2015.

Jiang, H., Farrar, J. T., Beardsley, Chen, R., and Chen, C. (2009), Zonal surface wind jets across the Red Sea due to mountain gap forcing along both sides of the Red Sea, Geophys. Res. Lett., 36, https://doi.org/10.1029/2009GL040008, 2009.

Johnson, B. T., Heese, B., McFarlane, S. A., Chazette, P., Jones, A., and Bellouin, N.: Vertical distribution and radiative effects of mineral dust and biomass burning aerosol over West Africa during DABEX, J. Geophys. Res., 113, https://doi.org/10.1029/2008JD009848, 2008.

Kahn, R. A., Gaitley, B. J., Martonchik, J. V., Diner, D. J., Crean, K. A., and Holben, B.: Multiangle Imaging Spectroradiometer (MISR) global aerosol optical depth validation based on 2 years of coincident Aerosol Robotic Network (AERONET) observations, *J. Geophys. Res.*, 110, https://doi.org/10.1029/2004JD004706, 2005.

Kalenderski, S. and G. Stenchikov, G.: High-  resolution regional modeling of summertime transport and impact of African dust over the Red Sea and Arabian Peninsula, J. Geophys. Res. Atmos., 121, 6435–6458, https://doi.org/10.1002/2015JD024480, 2016.

Khan, B., Stenchikov, G., Weinzierl, B., Kalenderski, S., and Osipov, S.: Dust plume formation in the free troposphere and aerosol size distribution during the Saharan Mineral Dust Experiment in North Africa, Tellus B Chem. Phys. Meteorol., 67, https://doi.org/10.3402/tellusb.v67.27170, 2015.

Kim, D., Chin, M., Kemp, E.M., Tao, Z., Peters-KAUST–MPLd, C.D., and Ginoux, P.: Development of high-resolution dynamic dust source function – A case study with a strong dust storm in a regional model, Atm. Environ., 159, 11–25, http://dx.doi.org/ 10.1016/j.atmosenv.2017.03.045, 2017.

Kim, M.-H., Omar, A. H., Tackett, J. L., Vaughan, M. A., Winker, D. M., Trepte, C. R., Hu, Y., Liu, Z., Poole, L. R., Pitts, M. C., Kar, J., and Magill, B. E.: The CALIPSO version 4 automated aerosol classification and lidar ratio selection algorithm, Atmos. Meas. Tech., 11, 6107–6135, https://doi.org/10.5194/amt-11-6107-2018, 2018.

Klose, M. and Shao, Y.: Stochastic parameterization of dust emission and application to convective atmospheric conditions, Atmos. Chem. Phys., 12, 7309-7320, https://doi.org/10.5194/acp-12-7309-2012, 2012.

Klose, M., and Shao, Y.: Large-eddy simulation of turbulent dust emission, Aeol. Res., 8, 49-58, https://doi.org/10.1016/j.aeolia.2012.10.010, 2013.

Koffi, B., Schulz, M., Bréon, F.M., Griesfeller, J., Winker, D., Balkanski, Y., Bauer, S., Berntsen, T., Chin, M., Collins, W.D., and Dentener, F.: Application of the CALIOP layer product to evaluate the vertical distribution of aerosols estimated by global models: AeroCom phase I results, J. Geophys. Res., 117, https://doi.org/10.1029/2011JD016858, 2012.

Kok, J.F., Ridley, D.A., Zhou, Q., Miller, R.L., Zhao, C., Heald, C.L., Ward, D.S., Albani, S. and Haustein, K.: Smaller desert dust cooling effect estimated from analysis of dust size and abundance, Nature Geosci., 10**,** 274–278, https://doi.org/10.1038/ngeo2912, 2017.

Kumar, R.K., Attada, R., Dasari, H. P., Vellore, R. K., Abualnaja, Y. O., Asok, K., and Hoteit, I.: On the recent amplification of dust over the Arabian Peninsula during 2002 – 2012, J. Geophys. Res. Atmos., 124, 13220-13229, 2019.

https://doi.org/10.5194/acp-2020-444
Preprint. Discussion started: 8 July 2020



Lee, Y. H., Chen, K., and Adams, P. J.: Development of a global model of mineral dust aerosol microphysics, Atmos. Chem. Phys., 9, 2441-2458, https://doi.org/10.5194/acp-9-2441-2009, 2009.

Lee Y. H. and P. J. Adams P. J.: A Fast and Efficient Version of the TwOMoment Aerosol Sectional (TOMAS) Global Aerosol Microphysics Model, Aerosol Science and Technology, 46, 678-689, https://doi.org/10.1080/02786826.2011.643259, 2012.

LeGrand, S. L., Polashenski, C., Letcher, T. W., Creighton, G. A., Peckham, S. E., and Cetola, J. D.: The AFWA dust emission scheme for the GOCART aerosol model in WRF-Chem v3.8.1, Geosci. Model Dev., 12, 131-166, https://doi.org/10.5194/gmd-12-131-2019, 2019.

Li, W., El-Askary, H., Qurban, M.A., Proestakis, E., Garay, M.J., Kalashnikova, O.V., Amiridis, V., Gkikas, A., Marinou, E., Piechota, T., and Manikandan, K.P.: An Assessment of Atmospheric and Meteorological Factors Regulating Red Sea Phytoplankton Growth, Remote Sens., 10, 673, http://dx.doi.org/10.3390/rs10050673., 2018.

Lopatin, A., Dubovik, O., Chaikovsky, A., Goloub, P., Lapyonok, T., Tanré, D., and Litvinov, P.: Enhancement of aerosol characterization using synergy of lidar and sun-photometer coincident observations: the GARRLiC algorithm, Atmos. Meas. Tech., 6, 2065–2088, https://doi.org/10.5194/amt-6-2065-2013, 2013.

Mahowald, N.M., Muhs, D.R., Levis, S., Rasch, P.J., Yoshioka, M., Zender, C.S. and Luo, C. (2006), Change in atmospheric mineral aerosols in response to climate: Last glacial period, preindustrial, modern, and doubled carbon dioxide climates, J. Geophys. Res., 111, https://doi.org/10.1029/2005JD006653.

Marenco, F., Ryder, C., Estellés, V., O'Sullivan, D., Brooke, J., Orgill, L., and Gallagher, M.: Unexpected vertical structure of the Saharan Air Layer and giant dust particles during AER-D, Atmos. Chem. Phys., 18, 17655-17668, https://doi.org/10.5194/acp-18-17655-2018, 2018.

Miller, S. T. K., Keim, B. D., Talbot, R. W., and Mao, H. ( 2003), Sea breeze: Structure, forecasting, and impacts, *Rev. Geophys.*, 41, 1011, https://doi.org/10.1029/2003RG000124, 2003.

Monahan E.C., Spiel D.E., and Davidson K.L.: A Model of Marine Aerosol Generation Via Whitecaps and Wave Disruption, in Oceanic Whitecaps, edited by Monahan E.C. and Niocaill G.M., Oceanographic Sciences Library, Springer, Dordrecht, 2, 167–174, https://doi.org/10.1007/978-94-009-4668-2_16, 1986.

Neuman, C.M., Boulton, J.W. and Sanderson, S.: Wind tunnel simulation of environmental controls on fugitive dust emissions from mine tailings, Atmospheric Environment, *43*, 520-529, https://doi.org/10.1016/j.atmosenv.2008.10.011, 2009.

Osipov, S., Stenchikov, G., Brindley, H., and Banks, J.: Diurnal cycle of the dust instantaneous direct radiative forcing over the Arabian Peninsula, Atmos. Chem. Phys., 15, 9537–9553, https://doi.org/10.5194/acp-15-9537-2015, 2015.

Osipov, S., and Stenchikov, G.: Simulating the regional impact of dust on the Middle East climate and the Red Sea, J. Geophys. R. Oceans, 123, 1032– 1047, https://doi.org/10.1002/2017JC013335, 2018.

Prakash, P. J., G. Stenchikov, S. Kalenderski, S. Osipov, and H. Bangalath (2015), The impact of dust storms on the Arabian Peninsula and the Red Sea (2015), Atmos. Chem. Phys., 15, 199–222, doi:10.5194/acp-15-199-2015, 2015.

Prospero, J. M.: Long- term measurements of the transport of African mineral dust to the southeastern United States: Implications for regional air quality, J. Geophys. Res., 104, 15917–15927, https://doi.org/10.1029/1999JD900072, 1999.

Ryder, C. L., Highwood, E. J., Walser, A., Seibert, P., Philipp, A., and Weinzierl, B.: Coarse and giant particles are ubiquitous in Saharan dust export regions and are radiatively significant over the Sahara, Atmos. Chem. Phys., 19, 15353–15376, https://doi.org/10.5194/acp-19-15353-2019, 2019.

Saide, P.E., Carmichael, G.R., Spak, S.N., Gallardo, L., Osses, A.E., Mena-Carrasco, M.A., and Pagowski, M.: Forecasting urban PM10 and PM2.5 pollution episodes in very stable nocturnal conditions and complex terrain using WRF–Chem CO tracer model, Atmos. Environ., 45, 2769-2780, https://doi.org/10.1016/j.atmosenv.2011.02.001, 2011.

Schepanski, K., Tegen, I., Laurent, B., Heinold, B., and Macke, A.: A new Saharan dust source activation frequency map derived from MSG- SEVIRI IR- channels, Geophys. Res. Lett., 34, https://doi.org/10.1029/2007GL030168, 2007.

Selezneva, E.S.: The main features of condensation nuclei distribution in the free atmosphere over the European territory of the USSR, Tellus, 18, 525-531, doi:10.1111/j.2153-3490.1966.tb00265.x, 1966.

Senghor, H., Machu, É., Hourdin, F., and Gaye, A. T.: Seasonal cycle of desert aerosols in western Africa: analysis of the coastal transition with passive and active sensors, Atmos. Chem. Phys., 17, 8395–8410, https://doi.org/10.5194/acp-17-8395-2017, 2017.

Senghor, H., Machu, É., Durán, L., Jenkins, G.S., and Gaye, A.T.: Seasonal Behavior of Aerosol Vertical Concentration in Dakar and Role Played by the Sea-Breeze, Open J. Air Pollut., 9, 11-26, http://dx.doi.org/10.4236/ojap.2020.91002, 2020.

Shao, Y., Wyrwoll, K.H., Chappell, A., Huang, J., Lin, Z., McTainsh, G.H., Mikami, M., Tanaka, T.Y., Wang, X., and Yoon, S.: Dust cycle: an emerging core theme in Earth system science, Aeol. Res., 2, 181–204, http://dx.doi.org/10.1016/j.aeolia.2011.02.001, 2011.

Simpson, J. E.: Sea breeze and local winds, Cambridge University Press, 1994.

Sokolik, I.N. and Toon, O.B.: Direct radiative forcing by anthropogenic airborne mineral aerosols. Nature, 381, 681–683, http://dx.doi.org/10.1038/381681a0, 1996.

Stephens, G., Winker, D., Pelon, J., Trepte, C., Vane, D., Yuhas, C., L'Ecuyer, T., and Lebsock, M.: CloudSat and CALIPSO within the A-Train: Ten Years of Actively Observing the Earth System, Bull. Amer. Meteor. Soc., 99, 569–581, https://doi.org/10.1175/BAMS-D-16-0324.1, 2018.

Teixeira, J.C., Carvalho, A.C., Tuccella, P., Curci, G., and Rocha, A.: WRF-chem sensitivity to vertical resolution during a saharan dust event, Phys. Chem. Earth Parts A/B/C, 94, 188-195, https://doi.org/10.1016/j.pce.2015.04.002, 2016.

Ukhov, A., Mostamandi, S., da Silva, A., Flemming, J., Alshehri, Y., Shevchenko, I., and Stenchikov, G.: Assessment of natural and anthropogenic aerosol air pollution in the Middle East using MERRA-2, CAMS data assimilation products,and high-resolution WRF-Chem model simulations, Atmos. Chem. Phys. Discuss., https://doi.org/10.5194/acp-2020-17, in review, 2020a.

Ukhov, A., Mostamandi, S., Krotkov, N., Flemming, J., da Silva, A., Li, C., Fioletov. V., McLinden, C., Anisimov, A., Alshehri, Y., and Stenchikov, G.: Study of SO2 pollution in the Middle East using MERRA- 2, CAMS data assimilation products, and high- resolution WRF- Chem simulations. J. Geophys. Res. Atmos., 125, e2019JD031993, https://doi.org/10.1029/2019JD031993, 2020b.

Wang, S.H., Lin, N.H., OuYang, C.F., Wang, J.L., Campbell, J.R., Peng, C.M., Lee, C.T., Sheu, G.R., and Tsay, S.C.: Impact of Asian dust and continental pollutants on cloud chemistry observed in northern Taiwan during the experimental period of ABC/EAREX 2005, J. Geophys. Res., 115, doi:10.1029/2009JD013692, 2010.

Welton, E.J., Campbell, J.R., Berkoff, T.A., Spinhirne, J.D., Tsay, S.C., Holben, B., Shiobara, M., and Starr, D.O.: The Micro-pulse KAUST–MPL Network (KAUST–MPL-Net), Twenty-first International Laser Radar Conference (ILRC21), Quebec City, Canada, 8-12 July 2002, https://ntrs.nasa.gov/search.jsp?R=20020083050, 2002.

Welton, E.J., Campbell, J.R., Spinhirne, J.D., and Scott III, V.S.: Global monitoring of clouds and aerosols using a network of micropulse KAUST–MPL systems, Proc. SPIE 4153, KAUST–MPL Remote Sensing for Industry and Environment Monitoring, Sendai, Japan, 13 February 2001, https://doi.org/10.1117/12.417040, 2001.

Wild, O., Zhu, X., and Prather, M. J.: Fast-J: accurate simulation of in- and below cloud photolysis in tropospheric chemical models, J. Atmos. Chem., 37, 245–282, https://doi.org/10.1023%2FA%3A1006415919030, 2000.

https://doi.org/10.5194/acp-2020-444
Preprint. Discussion started: 8 July 2020




Winker, D. M., Tackett, J. L., Getzewich, B. J., Liu, Z., Vaughan, M. A., and Rogers, R. R.: The global 3-D distribution of tropospheric aerosols as characterized by CALIOP, Atmos. Chem. Phys., 13, 3345–3361, https://doi.org/10.5194/acp-13-3345-2013, 2013.

Wu, L., Su, H., Kalashnikova, O. V., Jiang, J. H., Zhao, C., Garay, M. J., Campbell, J. R., and Yu, N.: WRF-Chem simulation of aerosol seasonal variability in the San Joaquin Valley, Atmos. Chem. Phys., 17, 7291–7309, https://doi.org/10.5194/acp-17-7291-2017, 2017.

Yuan, T., Chen, S., Huang, J., Zhang, X., Luo, Y., Ma, X., and Zhang, G.: Sensitivity of simulating a dust storm over Central Asia to different dust schemes using the WRF-Chem model, Atmos. Environ., 207, 16-29, https://doi.org/10.1016/j.atmosenv.2019.03.014, 2019.

Zhao, C., Ruby Leung, L., Easter, R., Hand, J., and Avise, J.: Characterization of speciated aerosol direct radiative forcing over California, J. Geophys. Res. Atmos., 118, 2372–2388, https://doi.org/10.1029/2012JD018364, 2013.

Zhang, Y., Liu, Y., Kucera, P. A., Alharbi, B. H., Pan, L., and Ghulam, A.: Dust modeling over Saudi Arabia using WRF-Chem: March 2009 severe dust case, Atmospheric Environment, 119, 118-130, https://doi.org/10.1016/j.atmosenv.2015.08.032, 2015.